Optics and Chemical Vapour Deposition of Graphene Monolayers on Various Substrates

Victor Yu
Centre for the Physics of Materials
Department of Physics
McGill University
Montréal, Québec
Canada

A Thesis submitted to the
Faculty of Graduate Studies and Research
in partial fulfillment of the requirements for the degree of
Master of Science

Contents

List of Figures

Abstract

Graphene-based devices are typically fabricated by exfoliation on substrates such as SiO_2/Si. This is a disordered surface which can degrade the intrinsic properties of graphene such as mobility. Hence, in order to optimize device performance, we investigated the possibility to deposit graphene on more ordered surfaces such as GaAs, despite the difficulty in locating exfoliated graphene on such substrates. We show that the optical contrast of graphene can be greatly enhanced by increasing the incident angle of the light on the substrates (SiO_2 and GaAs). In the second part, we move beyond the *standard* exfoliated graphene production to present a method for large-scale graphene synthesis by chemical vapour deposition (CVD). We varied various growth conditions to understand and optimize the mechanisms of graphene synthesis and the subsequent transfer techniques.

Résumé

Les dispositifs à base de graphène sont généralement fabriqués par exfoliation sur des substrats de SiO_2/Si, mais ces surfaces désordonnées peuvent dégrader les propriétés intrinsèques du graphène, comme la mobilité. Par conséquent, en vue d'optimiser la performance des dispositifs, nous avons étudié la possibilité de déposer le graphène sur des surfaces plus ordonnées, comme le GaAs, malgré la difficulté augmentée de l'identification du graphène exfolié sur ces surfaces. Nous démontrons que le contraste optique du graphène peut être grandement renforcé en augmentant l'angle d'incidence de la lumière sur les substrats (SiO_2 et GaAs). Dans la seconde partie, nous allons au-delà de la production *standard* du graphène exfolié pour présenter une méthode de synthèse de graphène à grande échelle par dépôt chimique en phase vapeur. Nous modifions les paramètres de croissance pour mieux comprendre et optimiser les mécanismes de croissance et les techniques de transfert subséquent.

Acknowledgments

I'd like to express my deep appreciation to my supervisor, Professor Michael Hilke. His intuition and broad knowledge have guided me to the right direction on such an active field and kept my motivation up throughout the Masters program. He has been very supportive of my research and gave me opportunities to present my research at local and international conferences. He also provided me with invaluable advice on paper writing, peer reviewing and presentation skills. Working in a quantum nanoelectronics group has expanded my horizons on various topics in mesoscopic physics.

Big thanks to our postdoc, Josianne Lefebvre for the correction of this thesis and her constant help, support and advice around the lab, especially, her meticulous contact making skills in wiring my CVD-grown graphene devices. Without her, this work would not be possible and I wouldn't know how most of the instruments in the lab work.

My deepest gratitude to our technician, Robert Gagnon for his technical skills and his teachings of practical skills such as machining the tilted stage for the work in Chapter 3 and setting up the CVD system for the graphene growth in Chapter 4.

Special thanks to Mathieu Massicotte and Eric Whiteway who helped me and will be pursuing some of my unfinished projects; Mathieu, for his aid in the preparation of the exfoliated graphene and Eric, for the CVD setup, growth and Raman analysis of Chapter 4.

Throughout my Masters, I also had the opportunity to collaborate with chemists and theorists. I would like to extend my thanks to Professor Mohammed Siaj, from chemistry at UQAM, for his pointers in successfully fabricating graphene devices and his graduate student, Abdelaadim Guermoune for great discussion about our results on the CVD-grown graphene from a chemist's point of view. Also, Jesse Masseen from Hong Guo's group who provided us a theoretical approach on the growth mechanism of graphene. This work would not be complete without the help of Dr. Samir Elouatik at Université de Montréal for the Raman system and Prof. Raynald Gauvin for the SEM of Materials and Mining Engineering at McGill.

Thanks to my former supervisor Prof. Thomas Szkopek who prepared me for the graduate program and also, providing us with graphite flakes and silicon wafers and also, to my former partner Jonathan Guillemette, who is now a graduate student of

Szkopek's group, helped me with the e-beam lithography system.

Thanks to the staff of the McGill Nanotools Microfab and Laboratoire de Microfabrication at l'École Polytechnique de Montréal for the training.

I would like to thank all my fellow physicists and friends to be part of my cooking sessions and making graduate life much easier and fun. Big thanks to those who kept my cooking blog *Random Cuisine* running for all those years and participated in the baking of the first ever graphene cake.

Finally, thanks to my brother, parents and family for their endless support even though they still don't understand what I do exactly for research.

Abbreviations and Symbols

AFM: Atomic Force Microscopy.
CMOS: Complementary Metal Oxide Semiconductor.
CCD: Charge-Coupled Device.
CVD: Chemical Vapour Deposition.
EM: Electromagnetic.
EBL: Electron Beam Lithography.
FET: Field Effect Transistor.
IPA: Isopropanol Alcohol.
iTO: in-plane Transverse Optical Phonon.
LA: Longitudinal Acoustic Phonon.
LO: Longitudinal Optical Phonon.
PMMA: Polymethylmethacrylate.
RIE: Reactive Ion Etching.
sccm: standard cubic centimeters per minute.
SEM: Scanning Electron Microscopy.
UHV: Ultra-high Vacuum.

1

Introduction

1.1 Introduction

Carbon emerges as one of the most remarkable elements found in a significant number of compounds. The most prevalent ones are the carbon allotropes and these can be classified according to their dimensionality. Graphite and diamond are examples of three-dimensional (3D) carbon structures that have been well known for centuries. Over the past two decades, research has been focused on zero-dimensional (0D) fullerenes[1] and one-dimensional (1D) carbon nanotubes[2] due to the ease in synthesizing these thermodynamically stable carbon structures. However, a single layer of graphite, known as graphene, was simply a theoretical model to understand the band structure of bulk graphite. It was predicted by Wallace in 1947 that graphene would have peculiar electrical and mechanical properties[3]. At that time, free standing graphene was presumed non-existant because 2D crystals are thermodynamically unstable at finite temperature[4].

This thermodynamic argument for 2D crystals is not applicable when a single layer graphene is bonded to a substrate such that graphene can indeed exist. It was only recently discovered that single layer graphene can be extracted from bulk graphite by mechanical cleavage and held on any types of substrates via Van der Waals interaction[5]. In 2004, Novoselov *et al.* made the first graphene-based measurable electronic device[6] and this discovery led to significant amount of interest in the study of graphene because of its high charge carrier mobility[7] and high mechanical strength[8], opening new doors for a wide-range of technological applications[9, 10, 11].

Here we will discuss the properties that contribute to these peculiar phenomena which has led to this year's Nobel prize in physics.

1.2 Morphology

Graphene is defined as a one atomic layer of carbon atoms densely packed in a honeycomb crystal lattice. Bilayer and few layer graphene consist of 2 and 3 to 10 layers of these 2D sheets, respectively. These carbon atoms can be arranged in a Bernal (AB) stacking or ABC stacking as illustrated in Fig. 1.1(a) and (b), respectively. Both these stackings have been observed experimentally[12]. Each carbon atom is bonded in-plane together with σ bonds, providing a solid hexagonal network while the out-of-plane π bonds accomplish the weak interaction between different graphene layers (Fig. 1.1(c)).

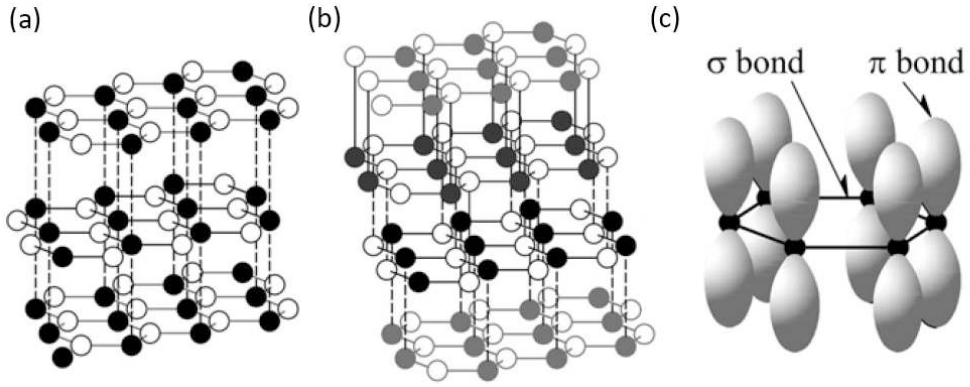

Figure 1.1: Two possible graphene stacking arrangements: (a) Bernal or AB stacking and (b) rhombohedral or ABC stacking. (c) Schematic of in-plane σ bonds and π orbitals perpendicular to the plane of the graphene sheets. Reproduced from [17].

1.3 Band Structure of Graphene

Single layer graphene consists of two carbon atoms per unit cell. Since the σ bonds are localized, they do not contribute to electronic conduction. We are mainly interested in the contribution of the delocalized π orbitals. The first Brillouin zone is a hexagonal cell in $\mathbf{k}$-space with high symmetry at the Γ, K and M points (Fig. 1.2(a)). The

dispersion relation of graphene is then calculated using a tight-binding model[3, 11], in which we consider only the first nearest-neighbour interaction which gives

$$E_{\pm}(\vec{\mathbf{k}}) = \pm t\sqrt{1 + 4\cos(\frac{\sqrt{3}k_x a}{2})\cos(\frac{k_y a}{2}) + 4\cos^2(\frac{k_y a}{2})} \tag{1.1}$$

where the lattice constant a = $\sqrt{3}$a$_0$, a$_0$ is the carbon-carbon bond length of 1.42Å and t is the nearest neighbour hopping energy of about 2.8 eV. The minus sign represents the valence π band whereas the plus sign is the conduction π^* band. The calculated band structure is shown in Fig. 1.2(b). The peculiar feature is found near the K/K' points where the valence and conduction bands form two conical structure and their tips are on the K/K' points (Fig. 1.2(c)).

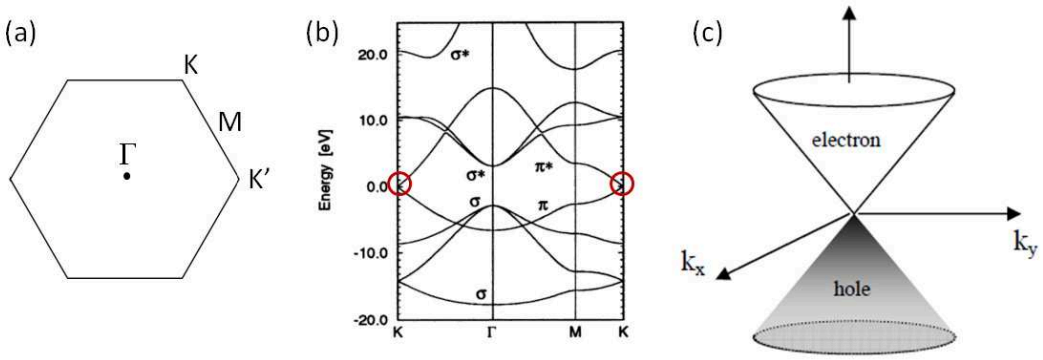

Figure 1.2: (a) Brillouin zone of graphene. (b) 2D band structure of graphene over the first Brillouin zone for the valence (π) and conduction (π^*) bands. Reproduced from [13]. (c) Linear dispersion, described by Dirac equations, found near the K and K' points (circled in red).

Unlike typical semiconductors in which charge carriers are described by the Schrödinger equation, the linear dispersion of graphene is described as a Dirac-like Hamiltonian where charge carriers behave like relativistic particles with a zero effective mass. Graphene is then defined as a zero-gap semiconductor and its linear dispersion Hamiltonian is obtained by expanding Eq.1.1 to the first order

$$\hat{H} = \hbar v_F \begin{pmatrix} 0 & k_x - ik_y \\ k_x + ik_y & 0 \end{pmatrix} = \hbar v_F \vec{\sigma} \cdot \vec{k}. \tag{1.2}$$

where $\vec{\sigma}$=(σ_x, σ_y) represents the two Pauli matrices and $\vec{k}$ is the momentum of

the quasi-particles in graphene and the Fermi velocity $v_F = \frac{\sqrt{3}ta}{2\hbar} \approx 10^6$m/s signifies that the charge carriers propagate 300 times slower than the speed of light. As a consequence, this unique band structure brings new interesting physical properties. For instance, charge carriers can be switched continuously between electrons and holes[5, 10]. Also, mobilities depend weakly on temperature meaning that ultrahigh mobility, usually reached at low temperature in other 2D structures such as GaAs-based 2DEGs, is attainable at room temperature[14].

1.4 Synthesis

The first attempt at synthesizing monolayer graphite was realized in 1975 by Lang demonstrating the formation of single to multi-layered graphite by chemical vapour deposition (CVD) on single crystal platinum[15]. Unfortunately, this process was abandonned due to a lack of reproducibility in the results. Moreover, at that time, no beneficial application had been identified for that product due to the unavailable methods of transferring monolayer graphite from metallic to insulating substrates. No further investigation on this process was done. A repeatable synthesis of graphene via mechanical exfoliation was realized by Novoselov *et al.* in 2004 [5, 6]. This technique has been applied since then, along with efforts to produce large-scale graphene. A few physical and chemical methods to produce graphene are presented here. An up-to-date list of all the available graphene preparation techniques are found in Ref.[16].

1.4.1 Mechanical Exfoliation

Highly oriented pyrolytic graphite (HOPG) consists of many graphene sheets weakly bonded together by Van der Waals force. A piece of scotch tape is used to peel off the multiple layers of graphene from the bulk graphite. Afterwards, the tape is gently rubbed on top of a substrate with a soft tweezer to prevent damaging the graphene flakes and this tape is then carefully removed. This successful technique can provide high structural and electronic quality flakes as thin as single and few layers of graphene. However, it can only produce small flakes of graphene of the order of

10μm in diameter suitable for academic research but not for industrial applications as the deposition of thin layers is laborious and time-consuming.

1.4.2 Epitaxial Growth

A commonly used technique to produce graphene is on the surface of silicon carbide (SiC) wafers[17], which produces large-area graphene. This is realized by annealing at high temperature (>1250°C) in ultra-high vacuum (UHV)[18] or argon atmosphere[19]. This process sublimate sufficient Si to leave behind a carbon rich surface, resulting in the growth of 1-3 high quality graphene layers. The number of graphene layers is determined by the decomposition temperature used and the amount of Si evaporated.

Even though this process looks attractive, a good control on the number of graphene layers has to be resolved. Another issue is the strong interaction between graphene and SiC and large difference in the thermal expansion coefficient of graphene and SiC that affect the electronic properties of graphene. Therefore, transport measurements of epitaxial graphene differ greatly from the one of mechanically exfoliated graphene[17, 20].

In a similar approach, graphene monolayers can be formed on the surface of transition metals via chemical vapour deposition (CVD). These are produced either by thermal decomposition of hydrocarbons undergoing a dehydrogenation process in which the carbon atoms rearrange into a honeycomb lattice[21] or by controlled segragation in which carbon atoms outdiffuse from the bulk of the substrate[22]. Further details about this approach are later discussed in this thesis.

1.4.3 Unzipping Carbon Nanotubes

A recent development on synthesizing graphene nanoribbons is to open up longitudinally multi-walled carbon nanotubes (MWNTs). This has been realized in three different ways[23, 24, 25]. The simplest approach is to partially enclose the carbon nanotubes with a polymer film. The uncoated surface is then exposed to a plasma etchant, unzipping the MWNTs into graphene nanoribbons[25]. This direct method

permits the production of scalable and well-controlled widths of graphene nanoribbons for electronic device fabrication purposes.

1.5 Motivation

The exceptional high mobility of graphene has attracted much interest in the scientific community and many potential applications have been proposed. One of them is the use of graphene as a high speed electronic device. However, disorder such as surface residues, charged impurities and ripples limit the device performance. Up until now, graphene devices have been fabricated on silicon substrate with a specific oxide thickness because single to few layers are identifiable on this type of substrate. Due to the highly disordered nature of SiO_2(Fig. 1.3), mobilities ranging from 1,000 to 20,000 $cm^2/V{\cdot}s$ have been obtained[26]. Higher mobilities can be achieved when the problem of sample disorder is overcome by suspending the graphene above the substrate, improving mobilities by more than one order of magnitude over devices on SiO_2[7]. However, making advanced devices out of suspended graphene is daunting considering the number of processing steps to acquire these results. In addition, mobilities of graphene on SiC range from 100 to 2,000 $cm^2/V{\cdot}s$ [19] and the low mobilities originate from the strong graphene-substrate interactions which has an impact on the electrical properties of graphene. Therefore, suspended-like or weakly interacting samples retain some intrinsic characteristics of graphene which minimize the number of scatterers in order to improve the device performance. This effect has been observed on ultraflat hexagonal boron nitride, where mobilities of 60,000$cm^2/V{\cdot}s$ has been achieved, three times more than SiO_2-supported devices[27].

The identification of graphene sheets down to single layer under an optical microscope makes device preparation easier and efficient. However, a strong contrast of graphene is only observed on specific substrates of specific thicknesses, thus limiting fabrication of devices to these substrates. For instance, high contrast of graphene is found on substrates such as SiO_2/Si, Si_3N_4/Si, SiC and Al_2O_3/Si. The observation of graphene on SiO_2/Si requires oxide thickness of 90, 285, or 465nm [28]; for Al_2O_3/Si

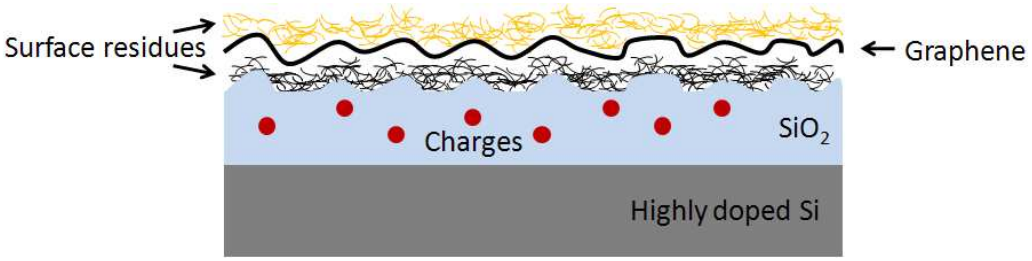

Figure 1.3: Schematic of disorder limiting the device performance.

72nm[29], and for Si_3N_4/Si 68nm[30]. A sample of typical contrast values of graphene deposited on a variety of substrates are found in Table 1.1. Typically, at contrasts less than 5%, graphene becomes almost invisible. Our goal is to integrate graphene on a variety of substrates in order to optimize its performance still providing sufficient contrast to identify the graphene sheets. Not much effort has been put into enhancing the contrast of graphene. The only proposed method is to coat graphene with a resist layer. This requires a very uniform resist before localizing the flakes of interest. In our work, we proposed a method to enhance the weak contrast of graphene on substrates such as GaAs which provides a smoother and cleaner surface. Localization of graphene flakes is usually realized under an inspection microscope at normal incidence. By changing the incident angle, the contrast of graphene can be enhanced depending on the choice of polarization and optical filters.

In addition, we are also interested in improving the mobilities and qualities of large-scale graphene grown on Cu foil. Current mobilities of grown graphene then subsequently transferred to SiO_2 are lower than those measured for mechanically exfoliated[21]. As large-scale CVD-grown graphene is still at its infant stage, these mobilities can still be improved by optimizing the synthesis, transfer and postprocessing. We will present some of our results of the synthesis of graphene as well as methods to transfer graphene from one substrate to another, providing a new way to manipulate graphene. This will guide us for future optimization on the quality of graphene and processings.

Table 1.1: Summary of the contrast of graphene on different substrate (Ref. [31]).

Type	Substrate	Max Contrast
Insulator	SiO_2	-0.1277
	Si_3N_4	-0.0438
	HfO_2	-0.0403
	Al_2O_3	-0.0664
	MgO	-0.0692
	TiO_2	-0.0456
TCO	ITO	-0.0457
Semiconductor	Si	-0.0066
	Ge	-0.0036
	GaAs	-0.0059
	GaN	-0.0266
	ZnO	-0.0394
	ZnSe	-0.0169
Metal	Co	0.0134
	Ni	0.0168
	Fe	0.0130
	NiFe	0.0147
	Au	0.0270
	Cu	0.0233

1.6 Thesis Organization

In the first part of Chapter 2, the theory of Raman scattering is introduced both in the classical and quantum picture. Raman spectra of the individual layers of graphene are presented in details along with an explanation of the Raman modes (D, G, and 2D). The second part of Chapter 2 presents the electron beam lithography system and optimal procedure to fabricate graphene-based devices efficiently. Chapter 3 provides the theory to compute the expected contrast of graphene applying the transfer matrix method and experiments confirming our predictions. Chapter 4 focuses on our chemical vapour deposition system used to synthesize graphene as well as some preliminary results on transferring graphene on insulating substrates. Finally, Chapter 5 summarizes the main results presented in this thesis.

2

Instrumentation and Sample Preparation

2.1 Raman Spectroscopy of Single and Few-Layer Graphene

A prompt and precise method for determining the number of layers of graphene is needed for research advancements and exploitation of graphene. Many techniques such as atomic force microscopy[32] and quantum Hall probing [10] are often used to distinguish a monolayer from a few-layer graphene. The former method leads to an inaccuracy on the thickness of graphene due to edge effects and the latter requires processing and ohmic contacts. In contrast, Raman spectroscopy is a non-destructive and powerful tool to characterize accurately the number of layers[33]. Here, we will describe the principles behind Raman spectroscopy, followed by an explanation of the individual components of the instrument, and finally a description of the characteristic peaks in graphene.

2.1.1 Classical Theory of Raman Scattering

A photon with frequency ν_0 is described as an electromagnetic wave which induces a dipole moment on the molecule. The strength of the induced dipole moment, P, is given by

$$P = \alpha E \tag{2.1}$$

where α is the polarizability and E, the electric field produced by the incident electromagnetic wave. The polarizability depends on the molecular structure and nature of the bonds. In an applied electric field, electron clouds of large molecules

have a strong polarizability which is easily distorted. Small and compact molecules have a weak polarizability.

The electric field of an electromagnetic wave fluctuates with time, t:

$$E = E_0 \cos(2\pi\nu_0 t) \tag{2.2}$$

Thus, substituing Eq.2.2 into Eq.2.1, one obtains

$$P = \alpha E_0 \cos(2\pi\nu_0 t) \tag{2.3}$$

If the molecule is vibrating with frequency ν_m, the physical displacement dQ of the atoms about their equilibrium position is written

$$dQ = Q_0 \cos(2\pi\nu_m t) \tag{2.4}$$

For small displacements, the polarizability can be written as

$$\alpha = \alpha_0 + (\frac{\partial\alpha}{\partial Q})_0 dQ \tag{2.5}$$

Here, the polarizability α_0 is at equilibrium position, and $(\partial\alpha/\partial\mathrm{Q})_0$ is the rate of change of α with respect to the change in Q evaluated at equilibrium position.

Combining Eq.2.3 and Eq.2.4 into Eq.2.5, one obtains

$$P = \alpha_0 E_0 \cos(2\pi\nu_0 t) + \frac{1}{2}\frac{\partial\alpha}{\partial Q}_0 Q_0 E_0[\cos(2\pi(\nu_0 + \nu_m)t)\cos(2\pi(\nu_0 - \nu_m)t) \tag{2.6}$$

The leading term has the same frequency as the excited photon which accounts for Rayleigh scattering while the second term corresponds to Raman scattering for both anti-Stokes (ν_0 + ν_m) and Stokes (ν_0 - ν_m) processes[34]. Note that the necessary condition for Raman scattering is that the $(\partial\alpha/\partial\mathrm{Q})_0$ is non-zero. This means that the molecular motion is Raman-active only if the motion occurs with a change in polarizability.

2.1.2 Quantum Theory of Raman Scattering

A quantum picture of Raman scattering is described as an inelastic collision process where a photon is annihilated and creates a phonon and a Stokes photon. Alternatively, a photon together with an annihilated phonon creates an anti-Stokes photon. According to quantum theory, a photon is emitted or absorbed as a result of making a transition between two discrete energy levels. The photons are thus considered quantized. Here we assume that a molecule is a harmonic oscillator with a quantized vibrational energy

$$E_n = h\nu_m(n + \frac{1}{2}), \tag{2.7}$$

where ν_m is the vibrational frequency of the molecule and n is a quantum number which takes positive integer values.

An energy transfer occurs when the Bohr's frequency condition is satisfied

$$\Delta E = h\nu_m. \tag{2.8}$$

As a result, this transfer energy must satisfy the energy difference between the excited state E and ground state E_0

$$\Delta E = E - E_0. \tag{2.9}$$

Fig. 2.1 illustrates the quantum picture of Raman scattering. The virtual states are considered as intermediate states between the ground and first excited electronic state. In a Rayleigh scattering process, the scattered light does not change its frequency and the energy is conserved, whereas for Stokes scattering, the transition starts from the ground state and lands on a higher energy level, and vice-versa for anti-Stokes scattering. This Raman frequency shift represents the energy difference between two vibrational levels which corresponds to the phonon's energy. This shift is an attribute relative to the material and is independent on the frequency of the emitted photon.

The signal from Raman scattering is generally weak, but it can be largely enhanced if the frequency of the incident photon is close to the material's absorption band. Rather than exciting the molecule to the virtual state, this suggests that the molecule

is excited near the first excited electronic state which enhances the signal by several orders of magnitude. This helps to characterize samples with low concentration or very weak signal.

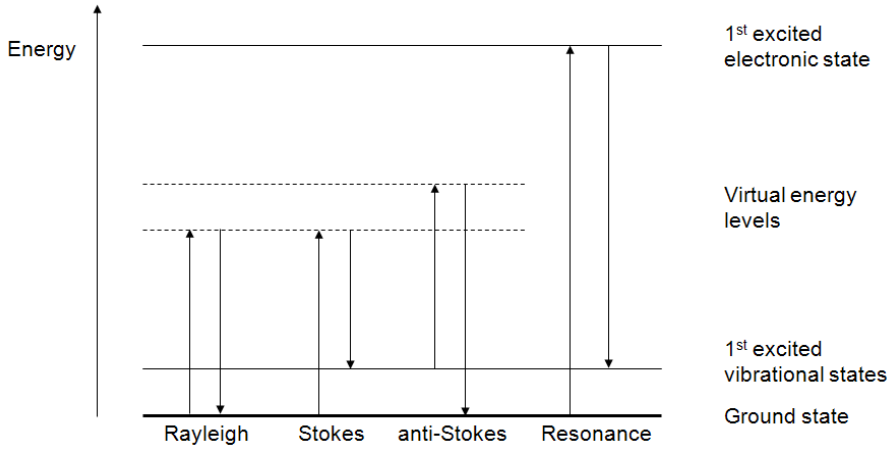

Figure 2.1: Rayleigh, Stokes, anti-Stokes and resonance scattering processes[35].

2.1.3 Polarizability

In a molecule, the polarizability α is a tensor quantity which consists of nine components (α_{xx}, α_{xy}, etc.). In a typical Raman scattering, the tensor is symmetric ($\alpha_{ij} = \alpha_{ji}$) so only six components are distinct. According to quantum mechanics, the vibration is Raman-active if one of these components in the tensor is changed during vibration, which is known as the Raman selection rules. Thus, in quantum mechanics, not all vibrational transitions will appear in the Raman spectrum due to symmetry argument provided by group theory[34, 35]. As for the classical picture, this theory breaks down since Eq.2.6 seems to suggest that all vibrational transitions are allowed as long $(\partial\alpha/\partial \mathrm{Q})_0$ is non-zero, indicating that there is no selection rules.

2.1.4 Raman Instrumentation

The Renishaw inVia Raman system was used in our experiment. This spectrograph consists of four main elements as illustrated in Fig. 2.2: an excitation source, a light detection system, a notch filter and an objective lens.

A white light source is employed to illuminate and focus on the sample. Four wavelengths (488, 514, 633 and 782 nm) are available in the Raman setup and any wavelength provides enough signal to measure the characteristic peaks of graphene. A 514nm laser is used to excite the sample through an objective lens. The spot size of the laser is about 350nm for a 100x objective lens with numerical aperture of 0.90. Typically, Raman measurements require average laser of the order of 10mWs. Increasing the laser power can suppress the background noise and enhance the resolution of the Raman peaks but the excessive heat can damage the sample. A sample is placed on a motorized stage which can move along the x- and y-axis, suitable for two-dimensional Raman mapping.

The Rayleigh signal is about 100 times stronger than the weak Raman signal. A notch filter is then used to reject this elastically scattered light and allows all the Raman scattered light to pass into the diffraction grating and be detected in the CCD camera. The Stokes shifts are measured in this manner. The data acquisition and analysis is realized using the WiRE software.

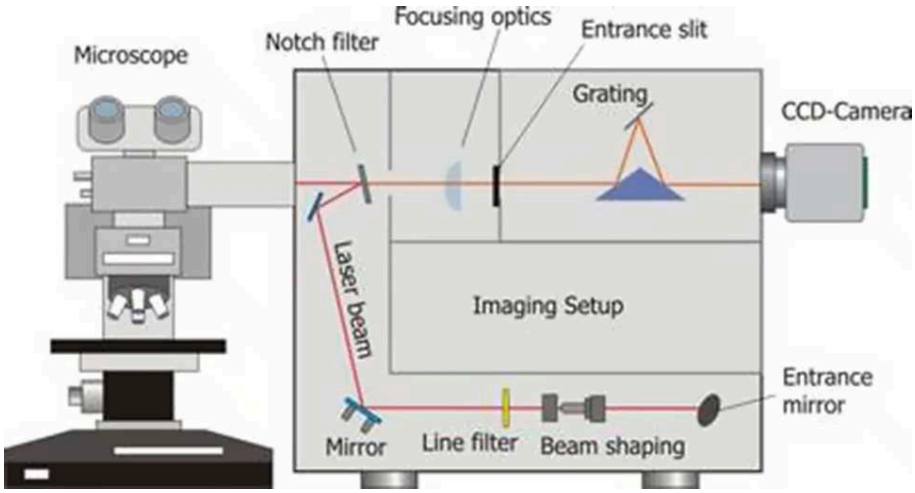

Figure 2.2: Diagram showing the individual components of the Renishaw Raman Microscopy system. Reproduced from [36].

2.1.5 Experimental Results on Graphene

The Raman spectra are measured with a 100x objective at 514nm, having a 1800 grooves/mm grating, available at Université de Montréal in the Chemistry Department. The laser power is set by default at 25 mWs. For optimal results, reduction of background noise and avoid sample damage, the detection time is set at 30 seconds at 10-50% power.

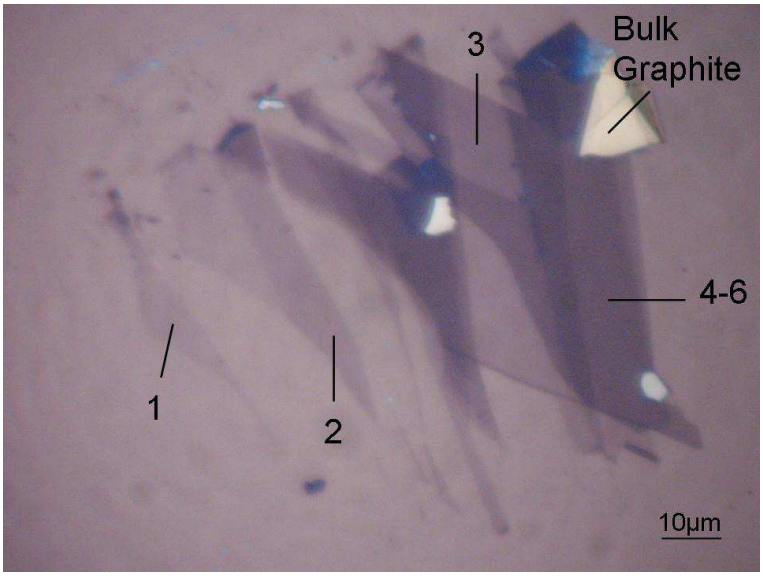

Figure 2.3: Optical image of graphene layers and graphite, indicating the corresponding number of layers and the regions where the Raman shifts data were measured.

Single to several layers of graphene were mechanically exfoliated and transferred onto a 90nm SiO_2/Si wafer as seen in Fig. 2.3. One can distinguish a graphene monolayer from several layer graphene by color interference, as will be explained in details in Chapter 3. Graphene monolayers are nearly transparent and additional layers lead to higher opacity. As a consequence, distinguishing two, three and few layered graphene by optical contrast is not easily achieved.

Under an optical microscope connected to the Raman spectrometer, Raman data were collected in each region indicated on Fig. 2.3. The Raman spectra of monolayer, bilayer, few layers of graphene and bulk graphite are summarized in Fig. 2.4. The D band at $\sim$1350 cm^{-1} is a breathing mode involving phonons near the K zone bound-

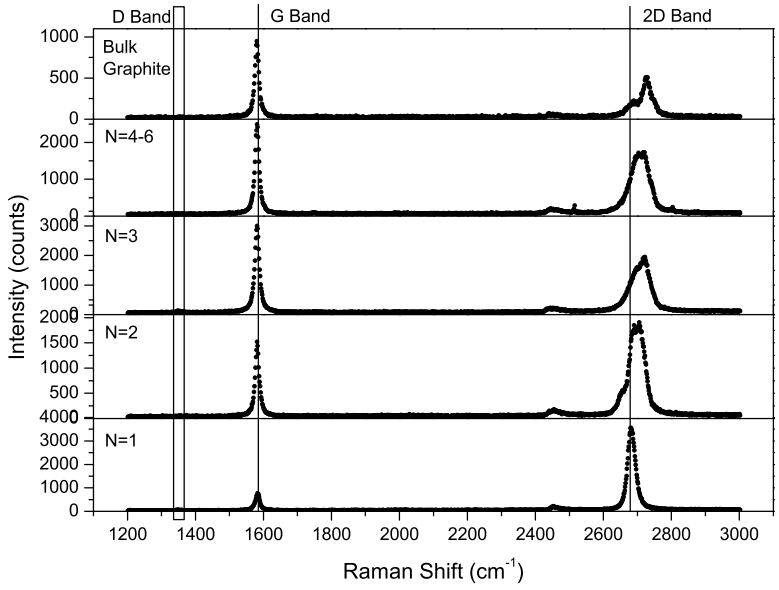

Figure 2.4: Raman spectra of one, two, three, few layers graphene and bulk graphite with its three signature peaks: D, G and 2D bands.

ary. This phonon mode (Fig. 2.5(a)) is forbidden in a perfect graphitic material and requires defects to be activated. The intensity of the D peak gives a good indication of the amount of disorder[37, 38]. The peak at ∼2450 cm^{-1}, assigned as G*, is described as a double-resonance process, involving one iTO and one LA phonon. Details about this peak are discussed in Refs.[39] and [40].

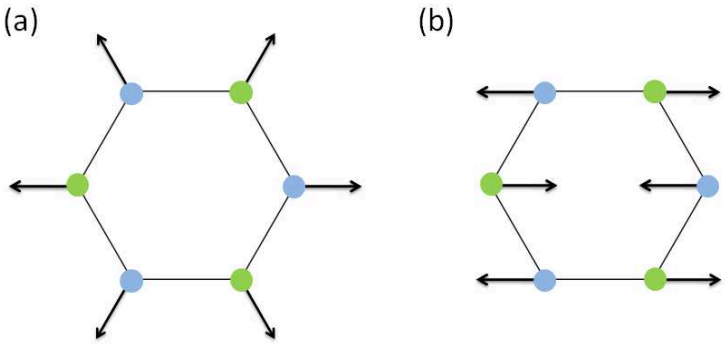

Figure 2.5: Representation of the graphene phonon modes: (a) D mode and (b) G mode

There are two characteristic peaks in the Raman spectra: the G peak at ∼1580cm^{-1}

and the 2D peak (also named G') located at ∼2700cm^{-1}. The G mode (Fig. 2.5(b)) represents the in-plane bond stretching of sp^2 carbon atom pairs, a doubly degenerate (iTO and LO) phonon mode at the center of the Brillouin zone[41]. The evolution of the 2D band is sensitive to the stacking order of graphite. A single layer graphene has a sharp 2D peak located at 2680cm^{-1} with a FWHM of ∼30cm^{-1}[40]. It is about 2-3 times more intense than the G peak depending on the substrate used and doping [42, 43] as shown in Fig. 2.4 for N=1. For a bilayer (N=2), the 2D band is composed of a superposition of 4 Lorentzian peaks. The key component involves the evolution of the graphene bands with the number of layers. One can explain the 2D band as a double-resonance process occuring along the Γ-K-M-K'-Γ direction in the first Brillouin zone, because the oscillation strength of the electron-phonon (π-iTO phonons) coupling near the K and K' points is significant[44, 45, 46]. Let's first analyse the case of a graphene monolayer as depicted in Fig. 2.6(a). The electronic structure consists of two bands: π and π*. The double-resonance process is described as follow: (i) a laser beam induces an electron/hole pair near K with energy E_{ex} (ii) the electron is scattered by a phonon with energy E_{ph} to a point adjacent to K' (iii) the electron is scattered back by another phonon near the K point (iv) a photon with energy E_{ex} - $2E_{ph}$ is emitted by electron-hole recombination. Since there is only one possible transition, the 2D band is a single symmetric peak corresponding to this double-resonance process.

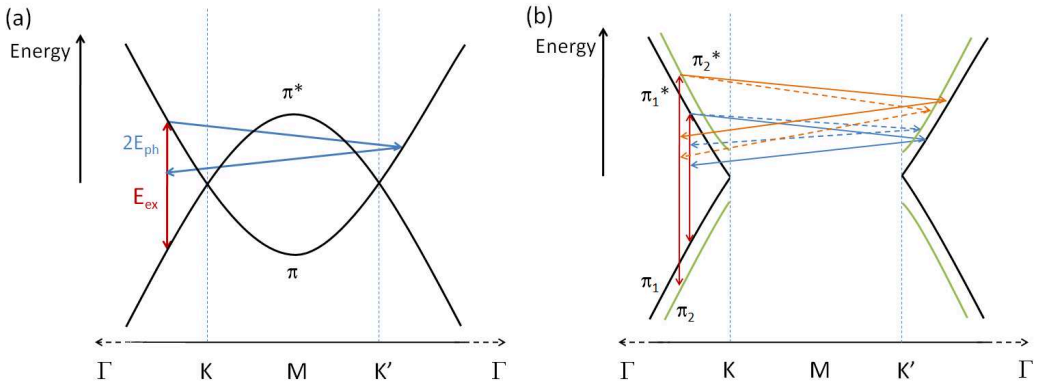

Figure 2.6: Double-resonance process for (a) single layer and (b) two layers graphene[46].

In order to understand the multiple peaks in the 2D band, the bilayer graphene case is analyzed. The dispersion curves of a bilayer are composed of four bands, two valence bands (π_1 and π_2) and two conduction bands (π_1* and π_2*). It is understood that the 2D band is fitted with four Lorentzian peaks [33, 40, 46, 47]. These peaks represent the four allowable optical transitions between the valence and conduction bands within the double-resonance process as depicted in Fig. 2.6(b). For clarity, the frequencies of these optical transitions are defined as ω_{11}, ω_{12}, ω_{21}, ω_{22}. For instance, ω_{12} is the frequency related to the transition in which the excited electron is on the π_1* at K, lands on π_2* at K' after phonon scattering, and scatters back to π_1*.

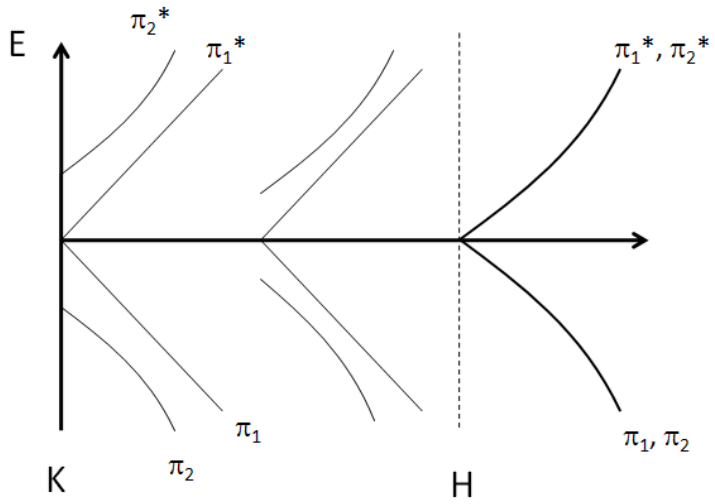

Figure 2.7: Evolution of the π electron dispersion curves along the K-H line.[46, 48]

For bulk graphite, it is represented as an infinite stacking of graphene sheets between the center and the top layer along the K-H line in the first Brillouin zone. Hence, electrons are scattered inelastically by phonons in that continuum of planes. The 2D band is then formed by a superposition of all possible optical transitions, giving rise to an infinite number of peaks. In order to understand the 2D band, one needs to observe the evolution of the π electron dispersion curves along the K-H line, represented in Fig. 2.7. According to Charlier *et al.*, the splitting between the two conduction bands as well as the two valence bands decreases as it approaches to the top plane. At H, the valence and conduction bands become degenerate [46, 48].

The 2D band of a bulk graphite is divided into one broad peak, centered at $\sim$2675cm^{-1} and one sharper peak at $\sim$2700cm^{-1} reflecting the evolution of the bands. The broad peak arises from the phonons with frequencies ω_{22}, ω_{21}, and ω_{12} which depend strongly on the splitting between the two valence bands and also, the two conduction bands. The values of these frequencies are modified as the electrons move along the K-H direction, resulting in an unlimited number of peaks. The sharp peak arises from the phonon with frequency ω_{11}. Unlike the other optical transitions, the π_2 and π_2* bands are not involved, thus the frequency ω_{11} remains unchanged and a sharp peak is expected.

2.2 Electron Beam Lithography for Graphene Field Effect Transistors

Graphene-based electronics has attracted much attention since the discovery of graphene due to its high carrier mobility. A basic graphene electronic device is a field effect transistor (FET); a device that consists of a source, a drain and a gate. Few of our graphene samples were succesfully contacted with electrodes. Moreover, these devices failed due to problems related to gate oxide leakage. As one of the first users of the Electron Beam Lithography (EBL) system in the McGill NanoTools Microfab, I spent a fair amount of time optimizing the success rate in patterning electrodes on micron-sized samples. I will first explain the basics of the EBL, followed by a description of the procedure for depositing electrodes on the sample and end by explaining important aspects that influences the lithographic process.

2.2.1 Basics of Electron Beam Lithography

Lithography is the process of transferring a pattern from one media to another. Photolithography applies light as a transfer media, ideal for large device production and industrial uses. On the other hand, electron beam lithography uses focused electrons to irradiate specific places on an electron-sensitive resist coating. This lithographic process consists of three steps: exposure to electrons, development of the resist and

pattern transfer. The resolution of submicron features is a combined effect of each of these individual steps. The end result and EBL operation are influenced by a great number of parameters and factors.

Direct writing EBL is based on a scanning electron microscope (SEM) equipped with a lithographic capability attachment. This complex system realizes a variety of structures with precise dimensions in determined locations. Briefly, the SEM, performed in ultra high vacuum conditions, provides a beam of electrons with a stable emission. A good control of the beam deflection provides precise operation of a user-defined pattern onto the sample, accurately positioned and dimensionally calibrated. In addition to this, beam blanking should be quick enough to avoid imprecision. All these requirements are ensured by a computer-based control system which manages all subsystems, rapidly and simultaneously.

2.2.2 Equipment

The McGill NanoTools Microfab is equipped with a SEM from Hitachi, model SU-70. It is based on a Schottky field emission filament, outstanding for its emission stability, convenient for lithography. The nomial resolution is 1 nm at 15keV and 1.6nm at 1keV. The acceleration voltage range is 0.1 - 30 kV, and the probing current ranges from 1pA to 100nA. Magnification ranges from 20x to 800kx. Secondary and backscattered electron detectors are used. Samples with a maximum diameter of 150mm can be introduced in the chamber and stage movements are motorized in X and Y.

Lithographic capabilities comprise an external beam blanker and a beam deflection system. The beam blanker abruptly deflects the beam by applying a voltage in the deflection coil. The Nanometer Pattern Generation System (NPGS) software controls the beam deflection, hardware for design, calibration and control of exposure conditions. The program is graphics-oriented and enables different configurations adapted to user preferences for each lithographic task.

2.2.3 *Sample Preparation Procedure*

A detailed process is explored here to optimize the fabrication of graphene FETs. The growth of a high quality oxide layer cannot be realized in the McGill Nanotools Microfab laboratory as it cannot produce CMOS-quality technology. High-quality wafers are better processed at University Wafer. For ultralow temperature measurements, a heavily-doped (n^{++}) <100> silicon wafer with resistivity in the range of mΩ·cm is recommended. At this high level of doping, arsenic is suggested as a dopant. A low-resistive micron-thick epitaxial layer growth is necessary to avoid any dopant propagation during the oxidation process which may affect the insulation of the oxide. A dry chlorinated thermal oxidation, as used in MOS, helps eliminate metal ions during SiO_2 growth. Since the oxide is formed on both sides of the wafer, the back oxide is etched by RIE if one needs to access the back gate.

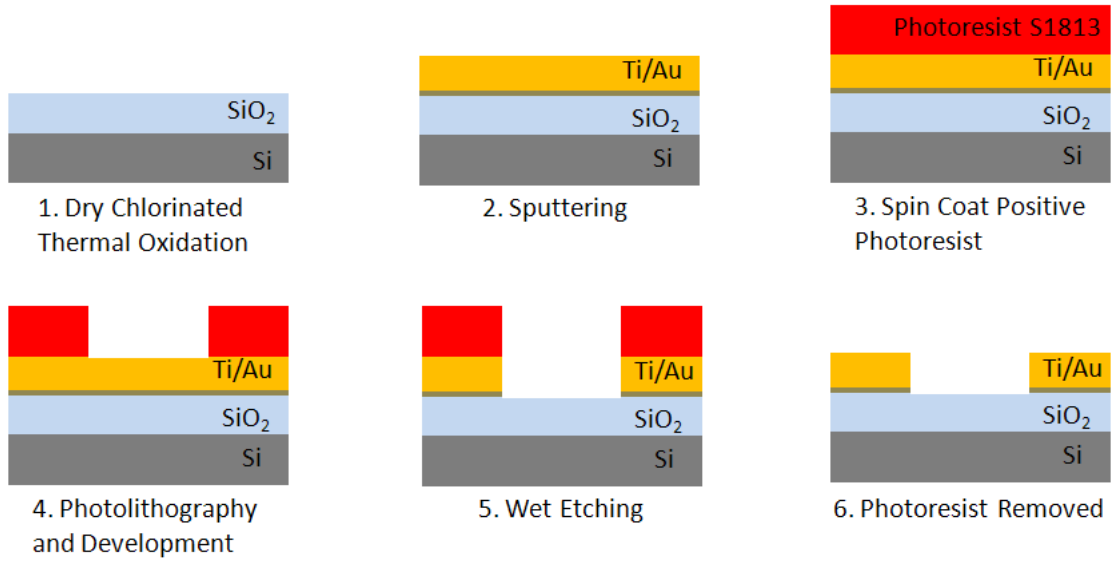

Figure 2.8: Process order of alignment deposition on SiO_2/Si substrate.

Alignment marks need to be made on the SiO_2/Si wafer to ease the lithographic process. The alignment marks deposition is shown in full details in Fig. 2.8. A 4-inch SiO_2/Si wafer is first sputtered with 10nm of titanium and 100nm of gold. As is done for photolithography, the wafer is spin coated with positive photoresist Shipley S1813 for 5 seconds at 500 rpm, then for 45 seconds at 1950 rpm, resulting in a 2.0 μm

resist layer. The photoresist is soft baked at 115°C for 60 seconds. The wafer is then placed inside the mask aligner with the use of a 5-inch photomask (labelled McGill 50767). The photomask consists of patterns such as crosses, alignment marks and bond pads that are exposed onto the resist with a dosage of 90mJ/cm^2. The resist is then developped for 60 seconds, removing the exposed regions.

The unaffected resist is employed as a mask for the wet etching process of the metals. The wafer is dipped in a diluted potassium-iodine-based solution to etch the gold layer. Because wet etching is an isotropic process, overetching results in the removal of the gold layer beneath the photoresist. The last step is a quick dip in 10:1 H_2O:HF solution to etch the titanium layer. The photoresist is then removed in hot acetone at 40°C. The end result is shown in Fig. 2.9.

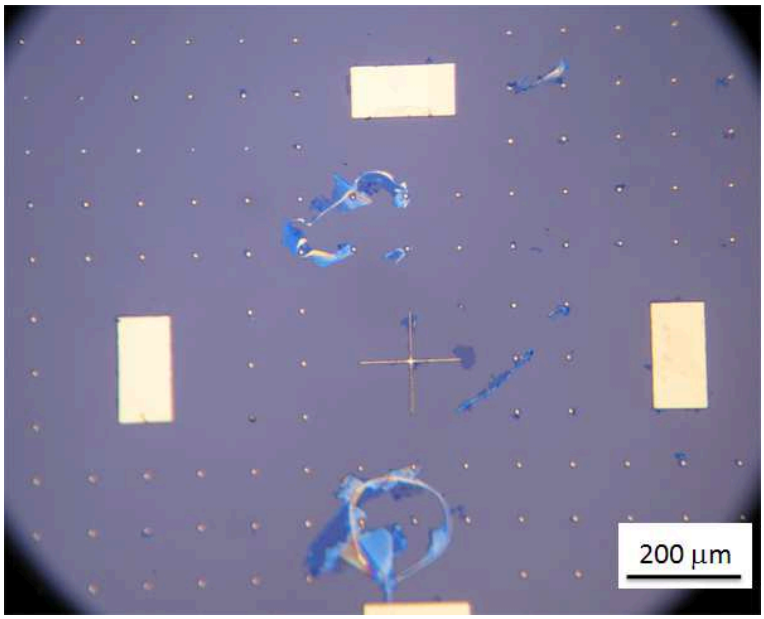

Figure 2.9: Alignment marks, bond pads and cross on SiO_2/Si wafer.

In order to perform electrical measurements in our system, the substrate needs to fit onto a 14-pin chip carrier, which means the wafer has to be cut. To prevent Si powder deposition on the surface of SiO_2 during dicing, a photoresist layer is spin coated on the wafer. A dicing saw is used to cut the wafer into 4mm × 6mm substrates and the photoresist is removed with acetone. The last step is to descum

the substrates inside the oxygen plasma asher for organic residues removal. These substrates are then exposed to oxygen plasma for 1 min at 100W.

2.2.4 *Exposure Procedure*

The procedure presented here is an improved version of the one provided by the Microfab (see Fig. 2.10). The lithographic procedure contains several steps: design of the pattern, setting of the beam parameters, calibration of the working field and stage positioning. For the version provided by the Microfab, the lithographic success rate depends strongly on the calibration for contacting micron-sized samples. Without proper calibration, the pattern is usually offset from the sample's location. The different calibrations are clarified in Appendix A.

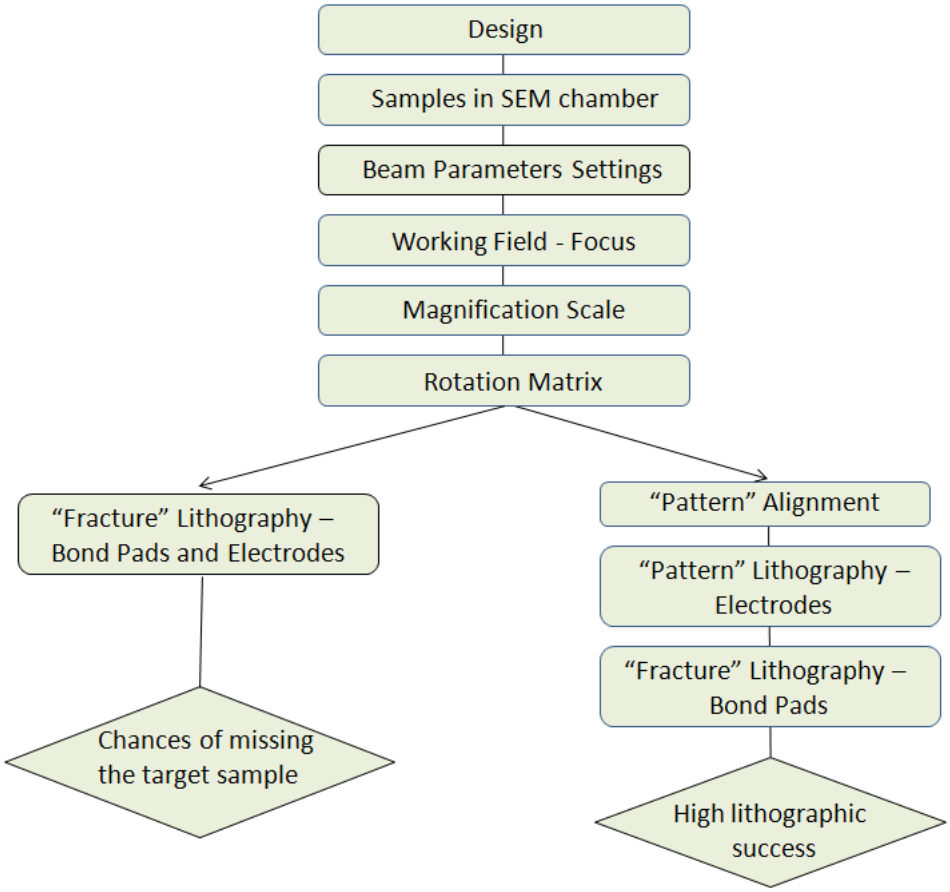

Figure 2.10: Schematic of the EBL procedures. Left column: Suggested method provided by the Microfab. Right column: Improved method

As for my version, it consists of more elaborated steps. To see this, the stage is positioned directly on the sample of interest with the aid of alignment marks that are closed to the sample. Electrodes are then drawn directly on the sample within the *Working Field*. This step does not involve any stage displacements and thus, no calibration is taken into account. Finally, extension of the electrodes to the bond pads is done by "Fracture" lithography which involves stage movement. The calibration is not as critical as the Microfab's version.

2.2.5 Electrode Deposition

The summary of the graphene FET processing is sketched in Fig. 2.11. In summary, graphene flakes are deposited by mechanical exfoliation, which then have to be located on the substrate. Optical images are captured at a magnification of 10x and 50x of the graphene flake for designing bond pads and electrodes respectively as discussed above. The designs are drawn in the DesignCad Express 16 software and are scaled with respect to the dimensions of the alignment marks. Full details of the procedure are found in Appendix B.

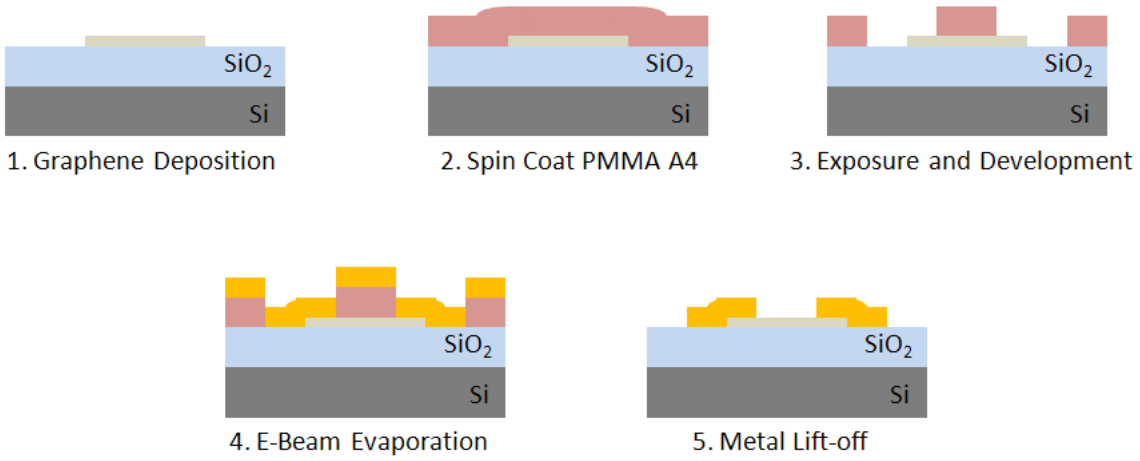

Figure 2.11: Fabrication process of graphene FETs.

For the electron beam exposure, the substrate is spin coated with an electron beam resist, polymethylmethacrylate (PMMA) A4 at 500 rpm for 5 seconds and at 4000 rpm for 45 seconds. It is then soft baked at 180°C for 60 seconds. The PMMA

thickness is about 175nm, sufficient to lift-out the metal with ease. The resist is then exposed by EBL according to the design with an area dose of 300.00 μm/cm^2. After exposure, the resist is then developed in 1:3 MIBK:IPA for 30-45 seconds.

An adhesive layer of 10nm of titanium, followed by a layer of 100nm of gold are evaporated using an electron beam evaporator. The sample is then left in a bath of acetone for a couple of hours to lift-off the metal. Finally, the substrate is placed on a chip carrier and the bond pads are wire-bonded to the pads of the carrier with aluminium wires as shown in Fig. 2.12.

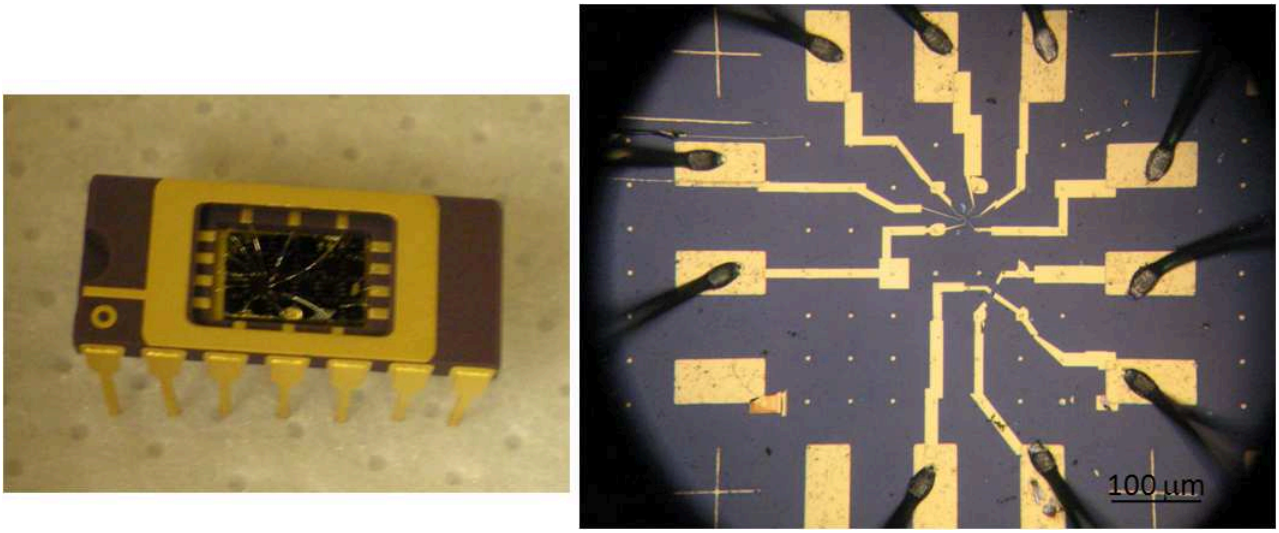

Figure 2.12: Left: Picture of a wire-bonded graphene device on a chip carrier. Right: Close-up image of two graphene flakes contacted with gold electrodes.

3

Contrast Enhancement of Graphene

The success in isolating a single layer graphene from highly oriented graphite via mechanical exfoliation has stimulated a large interest in both the fundamental properties and potential applications of graphene. As mentioned in Chapter 2, mechanically exfoliated graphite results in single and few layer graphene, and bulk graphite. Thus, before any device fabrication, the first step is to identify the number of layers of the graphene flakes and determine their relative position with respect to the alignment marks on the substrate. In order to realize this step, graphene needs to be observable with the naked eye under an optical microscope. So far, graphene flakes have been deposited on SiO_2/Si because of its sufficient contrast to this substrate[28, 30, 49, 50, 51]. However, it is also of interest to deposit on other types of substrates on which graphene becomes almost invisible under an optical microscope. In this chapter, we will present our published work on enhancing the visibility of graphene on substrates by angle detection[52]. Both the theoretical and experimental aspects are presented here.

3.1 Overview of EM Waves

The visibility of a material is related to the interaction of an electromagnetic (EM) wave with electrons in materials. For a metal, the free electrons tend to move in phase with an EM wave such that reflection occurs, whereas in an insulating material, transparency arises from a weak interaction of the electrons. This modifies the relative phase shift of the EM wave. We will first present an overview of Maxwell's equations in matter, then an explanation of the behaviour of an EM wave in different media

and then finish the discussion on how the reflectance changes under transverse electric (TE) and transverse magnetic (TM) polarizations.

3.1.1 Maxwell's Equations in Matter

Maxwell's equations describe the behaviour of an electromagnetic wave in response to a charge density, ρ, and current density, $\mathbf{J}$. In vacuum, the four laws of electromagnetism can be stated as follow

$$\begin{aligned} \nabla \cdot \mathbf{E} &= \frac{\rho}{\varepsilon_0}, \\ \nabla \times \mathbf{E} &= -\frac{\partial \mathbf{B}}{\partial t}, \\ \nabla \cdot \mathbf{B} &= 0, \\ \nabla \times \mathbf{B} &= \mu_0 \varepsilon_0 \frac{\partial \mathbf{E}}{\partial t} + \mu_0 \mathbf{J}. \end{aligned} \tag{3.1}$$

Since we are interested in the optical properties of materials, the presence of a medium in electric and magnetic fields can lead to electric dipoles and magnetic moments, polarization charges and induced current. The introduction of the electric displacement $\mathbf{D}$ and the magnetic field $\mathbf{H}$ allows us to take into account modifications by the medium.

In a linear medium, the electric flux density $\mathbf{D}$ and electric field $\mathbf{E}$ are related by the dielectric constant ε_1. Likewise, the magnetic field $\mathbf{H}$ is linked to the magnetic induction $\mathbf{B}$ by the permeability μ_1. Since we are not using any magnetic materials, μ_1 is close to μ_0. Both equations can then be written as follow

$$\mathbf{D} = \varepsilon_1 \mathbf{E} \qquad \textit{and} \qquad \mathbf{B} = \mu_1 \mathbf{H}. \tag{3.2}$$

Thus, we can rewrite Maxwell's equations in matter as follow

$$\begin{aligned} \nabla \cdot \mathbf{D} &= \rho_f, \\ \nabla \times \mathbf{E} &= -\frac{\partial \mathbf{B}}{\partial t}, \\ \nabla \cdot \mathbf{B} &= 0, \\ \nabla \times \mathbf{H} &= \frac{\partial \mathbf{D}}{\partial t} + \sigma_1 \mathbf{E}, \end{aligned} \tag{3.3}$$

where σ_1 is the conductivity of the material.

3.1.2 Wave Equations in Matter

To solve Maxwell's equations in matter, we consider an infinite medium in which edge effects are neglected. A general solution is to consider that the electric and magnetic waves consist of a sinusoidal periodic time and spatial dependence

$$\mathbf{E}(\mathbf{r},t) = \mathbf{E_0}\exp\{i(\mathbf{q}\cdot\mathbf{r}-\omega t)\}, \tag{3.4}$$

and

$$\mathbf{H}(\mathbf{r},t) = \mathbf{H_0}\exp\{i(\mathbf{q}\cdot\mathbf{r}-\omega t)\}. \tag{3.5}$$

It is preferable to express $\mathbf{E}$ and $\mathbf{H}$ as waves with wavevector $\mathbf{q}$ and frequency ω propagating into the material. Hence, eliminating $\mathbf{D}$ and $\mathbf{B}$ from Eq.3.3 and assuming the absence of free charges ($\rho_f = 0$), the wave equation for the electric field can be written as

$$\nabla^2\mathbf{E} = \mu_1\varepsilon_1\frac{\partial^2\mathbf{E}}{\partial t^2} + \mu_1\sigma_1\frac{\partial\mathbf{E}}{\partial t}. \tag{3.6}$$

The first term in the right-hand side of Eq.3.6 represents Maxwell's displacement current, and the second term is due to the conduction current. Similarly, one obtains

$$\nabla^2\mathbf{H} = \mu_1\varepsilon_1\frac{\partial^2\mathbf{H}}{\partial t^2} + \mu_1\sigma_1\frac{\partial\mathbf{H}}{\partial t}, \tag{3.7}$$

describing the propagation of the magnetic field.

3.1.3 Complex Index of Refraction

When an EM wave propagates into a material with dielectric constant ε_1, permeability μ_1 and conductivity σ_1, these parameters change the behaviour of the fields. One can describe the optical properties of the medium as a complex refractive index defined as

$$\tilde{n} = n + i\kappa. \tag{3.8}$$

where the real index of refraction n and the extinction coefficient κ are used to describe the propagation and dissipation of EM waves in the material. In order to understand

their meanings, we will consider two cases of materials which will be employed later in this chapter: insulators and semiconductors.

In an insulator where the conductivity is negligible ($\sigma_1 = 0$), Eqs. 3.6 and 3.7 are reduced to recognizable wave equations:

$$\nabla^2\mathbf{E} = \mu_1\varepsilon_1\frac{\partial^2\mathbf{E}}{\partial t^2} \qquad and \qquad \nabla^2\mathbf{H} = \mu_1\varepsilon_1\frac{\partial^2\mathbf{H}}{\partial t^2}. \tag{3.9}$$

From these equations, the magnitude of $\mathbf{E}$ and $\mathbf{H}$ is not modified inside the material, but the wave propagates slower than a wave in vacuum. By definition, this reduced velocity is related to the real part of the refractive index

$$v = \frac{1}{\sqrt{\varepsilon_1\mu_1}} = \frac{c}{n}. \tag{3.10}$$

In a semiconductor or any non-metallic material ($\sigma_1 \neq 0$), when plugging Eq.3.4 into Eq.3.6, we obtain a relationship between $\mathbf{q}$ and the frequency ω:

$$\mathbf{q} = \omega\left[\varepsilon_1\mu_1 + i\frac{\mu_1\sigma_1}{\omega}\right]^{1/2}\hat{n}_{\mathbf{q}}, \tag{3.11}$$

where $\hat{n}_{\mathbf{q}}$ is the unit vector along the $\mathbf{q}$ direction. This is a compact way to express a complex wavevector $\mathbf{q}$. We can then link Eq.3.11 to the complex index of refraction $\tilde{n}$:

$$\tilde{q} = \omega\frac{\tilde{n}}{c} = \omega\frac{(n+i\kappa)}{c} = \omega\left[\varepsilon_1\mu_1 + i\frac{\mu_1\sigma_1}{\omega}\right]^{1/2}. \tag{3.12}$$

This illustrates that a wave propagating into a semiconductor, experiences a velocity change as well as an attenuation compared to when propagating in vacuum.

3.1.4 Absorption Coefficient

The absorption coefficient α defines on how easily the light penetrates into a material. This is defined as the portion of the power absorbed in a unit length of the medium. If light is propagating in the x direction, the intensity at x is $I(x)$, then the intensity decrease per slice is given by

$$dI = -\alpha dx \times I(x). \tag{3.13}$$

Solving this differential equation, we obtain a general equation known as **Beer's law**:

$$I(x) = I_0 \exp\{-\alpha x\}. \tag{3.14}$$

To illustrate this with EM waves, we start by substituing the complex wavevector $\mathbf{q}$ (Eq.3.12) into the sinusoidal wave (Eq.3.4), which splits into a real and an imaginary component

$$\mathbf{E} = \mathbf{E_0} \exp\left\{i\omega\left(\frac{n}{c}\hat{n}_\mathbf{q} \cdot \mathbf{r} - t\right)\right\} \exp\left\{-\frac{\kappa\omega}{c}\hat{n}_\mathbf{q} \cdot \mathbf{r}\right\}. \tag{3.15}$$

The first exponent describes a wave propagating with a reduced velocity c/n. The second exponent is the damping term in which the amplitude falls off with a decay constant of $\kappa\omega$. The same goes for the magnetic wave $\mathbf{H}$. Comparing this to Beer's law given in Eq. 3.14, we can conclude that

$$\alpha = \frac{\kappa\omega}{c} \tag{3.16}$$

From Eq.3.12, the extinction coefficient κ is related to the material's parameters ε_1, μ_1 and σ_1, and one obtains the compact form for the absorption coefficient

$$\alpha = \frac{\sigma_1\mu_1}{\mu_0 nc}. \tag{3.17}$$

Therefore, the absorption strongly depends on the conductivity σ_1; for instance, a small attenuation coefficient means that the material is nearly transparent, while in a highly conductive material, the wave quickly decays.

3.1.5 Boundary Conditions

Based on how waves behave inside a material, we will move on and include boundary conditions. When EM waves propagate from one medium to another, the values of ε_1 and μ_1 differ accordingly. A set of boundary conditions is needed to ensure that waves in the two media match at the boundary.

Since we will be dealing with insulators and semiconductors, we consider that the interface is continuous, ignoring surface and current charges. The boundary conditions between two media are then written as follows

$$\mathbf{n} \times (\mathbf{E_2} - \mathbf{E_1}) = 0 \tag{3.18}$$

$$\mathbf{n} \times (\mathbf{H_2} - \mathbf{H_1}) = 0 \tag{3.19}$$

where $\mathbf{n}$ is normal to the interface of the two media.

3.2 Reflectance with a Non-Zero Incident Angle

The reflectance is defined as the intensity of light that is reflected from the material. Previous groups that have calculated the reflectance of graphene on substrates have focused only the effect at normal incidence[28, 30, 49, 51]. Here, we consider two media with index of refraction $\tilde{n_1}$ and $\tilde{n_2}$ and a wave entering the medium at an incident angle θ_i. A fraction of the wave is reflected at an angle θ_r and transmitted at an angle θ_t. We will prove that indeed the reflectance does depend on the angle of incidence when $\theta_i \neq 0$; $\theta_i = 0$ describing normal incidence[53].

3.2.1 TE Polarization

TE polarization refers to the electric field vector $\mathbf{E}$ perpendicular to the plane of incidence as shown in Fig. 3.1

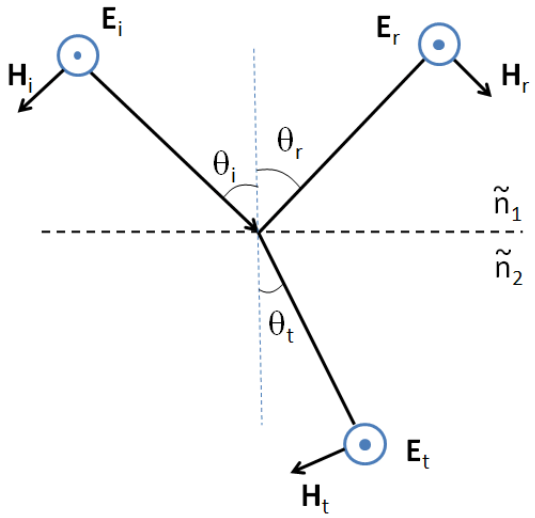

Figure 3.1: Diagram representing the electric and magnetic field components of TE polarization.

We can then rewrite the boundary conditions from Eqs 3.18 and 3.19

$$E_i + E_r = E_t \tag{3.20}$$

$$(-H_i + H_r)\cos\theta_i = -H_t \cos\theta_t \tag{3.21}$$

Defining the impedance as the ratio of the electric and magnetic components due to the influence of the medium. For instance, the impedance of medium 1 can be written as

$$z_1 = \frac{E_1}{H_1} = \sqrt{\frac{\mu_1\mu_0}{\varepsilon_1\varepsilon_0}} = \frac{z_0}{\tilde{n}_1} \tag{3.22}$$

where z_0 is the impedance in free space.

Combining Eqs. 3.20, 3.21 and 3.22, one obtains the reflectance R by taking the ratio of the amplitude of E_r by E_i

$$R = \left|\frac{E_r}{E_i}\right|^2 = \left|\frac{\tilde{n}_2\cos\theta_t - \tilde{n}_1\cos\theta_i}{\tilde{n}_2\cos\theta_t + \tilde{n}_1\cos\theta_i}\right|^2 \tag{3.23}$$

3.2.2 TM Polarization

A similar analysis can be performed for TM polarization, for which the magnetic field is parallel to the interface as sketched in Fig. 3.2.

The boundary conditions are then written as follows

$$(E_i + E_r)\cos\theta_i = E_t\cos\theta_t, \tag{3.24}$$

$$H_i + H_r = H_t. \tag{3.25}$$

Combining Eqs.3.24 and 3.25 with the impedance in Eq.3.22, the reflectance which is the portion of light that is reflected is then given by

$$R = \left|\frac{\tilde{n}_1\cos\theta_t - \tilde{n}_2\cos\theta_i}{\tilde{n}_1\cos\theta_t + \tilde{n}_2\cos\theta_i}\right|^2. \tag{3.26}$$

Now that we have a sense on how the reflectance depends on incident angles under both TE and TM polarizations, we will provide a model to compute the contrast of graphene deposited on a multilayered substrate.

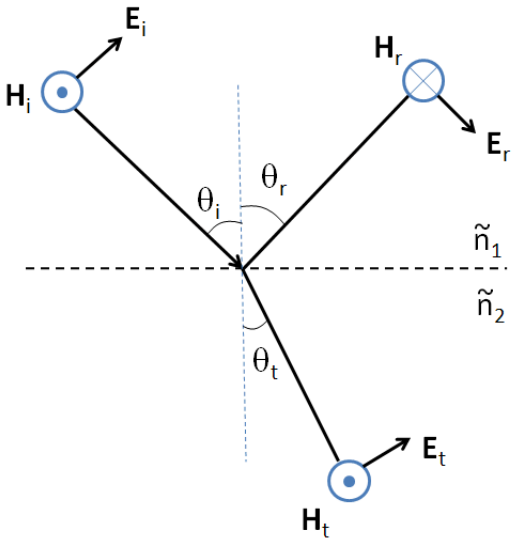

Figure 3.2: Diagram representing the electric and magnetic field components of TM polarization.

3.3 Contrast of Graphene on SiO_2/Si substrate

The visibility of graphene deposited on substrates originates from the modification of the relative phase shift and amplitude induced by the graphene layer. We compute the contrast of graphene on a SiO_2/Si substrate with an oxide thickness of 90nm and graphene thickness set to 0.34nm. We then consider an incoming light beam of wavelength λ, which hits a trilayer structure (graphene/SiO_2/Si) and passes through a series of reflections and transmissions as depicted in Fig. 3.3. The Si layer is considered semi-infinite and characterized by a complex index of refraction $\tilde{n}_3$ that is dependent on wavelength λ. For instance, at $\lambda = 400$nm, the index of refraction is $\tilde{n}_3(400\text{ nm}) = 5.57 + 0.39\text{i}$. SiO_2 is an insulator which also has a λ-dependent index of refraction but without an imaginary part $\tilde{n}_2(400\text{ nm}) = 1.47$. These values can be found in Refs. [54, 55]. The index of refraction of graphene is assumed to be close to that of bulk graphite and is λ-independent, i.e. $\tilde{n}_1(\lambda) = 2.6 + 1.3\text{i}$.

The results are obtained by considering a system of three layers (Fig. 3.3) in which each layer j can be represented by a transfer matrix. Here we assume that the wave is traveling in the xy plane. For a TM polarization, the magnetic field component H^z is parallel to the layers and the electric component E^y is at the incident angle θ. The

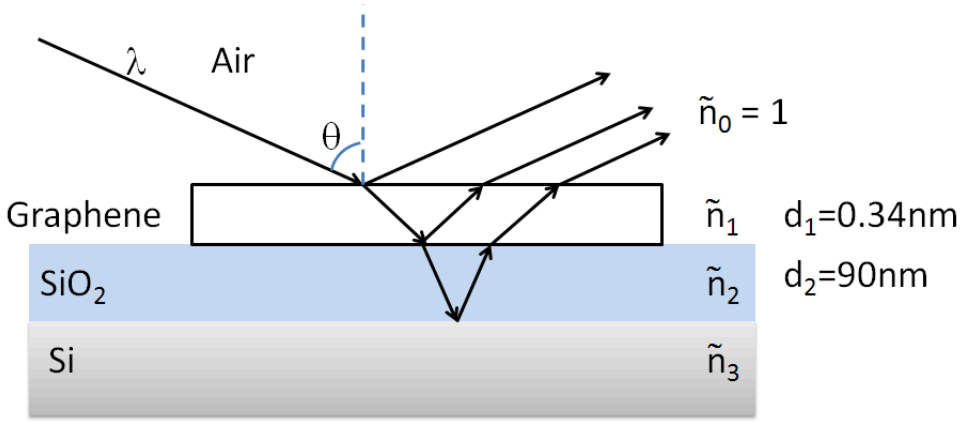

Figure 3.3: Schematic of light reflection for three-layer system.

general form of the transfer matrix for a layer j can be written as[56]

$$\begin{pmatrix} H_{j-1}^z \\ E_{j-1}^y \end{pmatrix} = \underbrace{\begin{pmatrix} \cos(\phi_j) & -i\sin(\phi_j)/\gamma_j \\ -i\sin(\phi_j)\gamma_j & \cos(\phi_j) \end{pmatrix}}_{M_j} \begin{pmatrix} H_j^z \\ E_j^y \end{pmatrix}. \tag{3.27}$$

The relation of the field components for a wavelength λ can be expressed as the product of transfer matrices

$$M = \prod_{j=1}^{2} M_j, \tag{3.28}$$

with the reflectance given by

$$R = \left| \frac{M_{11} + \gamma_3 M_{12} - M_{21}/\gamma_0 - \gamma_3 M_{22}/\gamma_0}{M_{11} + \gamma_3 M_{12} + M_{21}/\gamma_0 + \gamma_3 M_{22}/\gamma_0} \right|^2, \tag{3.29}$$

where M_{kl} are the matrix elements of M. The matrix M_j in Eq. 3.27 depends on the index of refraction ($\tilde{n}_j$) and thickness (d_j) of the corresponding layer, with phase shift

$$\phi_j = (2\pi d_j/\lambda)\sqrt{\tilde{n}_j^2 - \sin^2(\theta)}, \tag{3.30}$$

and

$$\gamma_j = (z_0/\tilde{n}_j^2)\sqrt{\tilde{n}_j^2 - \sin^2(\theta)}. \tag{3.31}$$

For a TE polarization, the expressions have to be substituted by $H^z \to E^z$, $E^y \to -H^y$, and $\gamma_j = z_0^{-1}\sqrt{\tilde{n}_j^2 - \sin^2(\theta)}$.

Once the reflectance is computed, the contrast is given by

$$C = \frac{R_{substrate} - R_{graphene}}{R_{substrate}}, \tag{3.32}$$

where $R_{substrate}$ is the reflectance without graphene and $R_{graphene}$, the reflectance in the presence of graphene.

3.3.1 Contrast of Graphene at Normal Incidence

Several groups have applied Fresnel's law to simulate the contrast of graphene at normal incidence [28, 30, 31] and their results concord well with each other. Instead, we have used a transfer matrix method (Eq. 3.27), which provides flexibility and simplicity in computing a generalized N-layer system with varying incident angle.

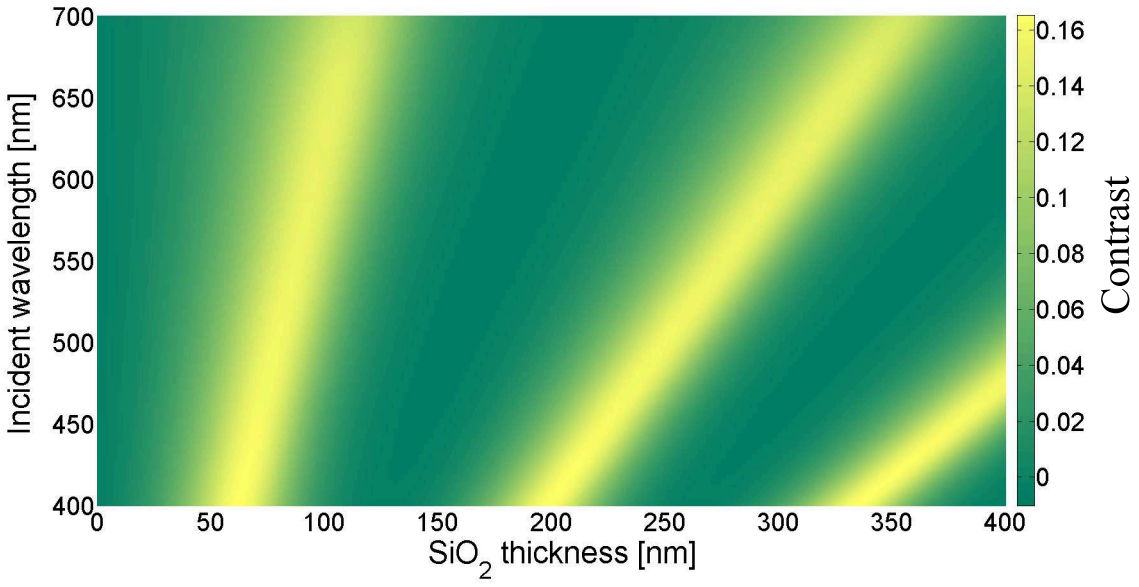

Figure 3.4: Contrast plot of graphene at normal incidence.

We have verified that the transfer matrix method (Eq. 3.27) is in good agreement with the results obtained by other groups using Fresnel's law. Indeed, we have plotted in a colour map, the contrast of graphene (Eq. 3.32) as a function of SiO_2 thickness and visible wavelength at normal incidence ($\theta = 0°$) as shown in Fig. 3.4. This provides a guide for the expected contrast of graphene when selecting a wavelength filter for a given thickness. Hence, optimal thicknesses of the oxide layer are found to

be 90 and 285nm with the use of green filters or white light. These lead to an optical contrast of about 15% for a single layer graphene.

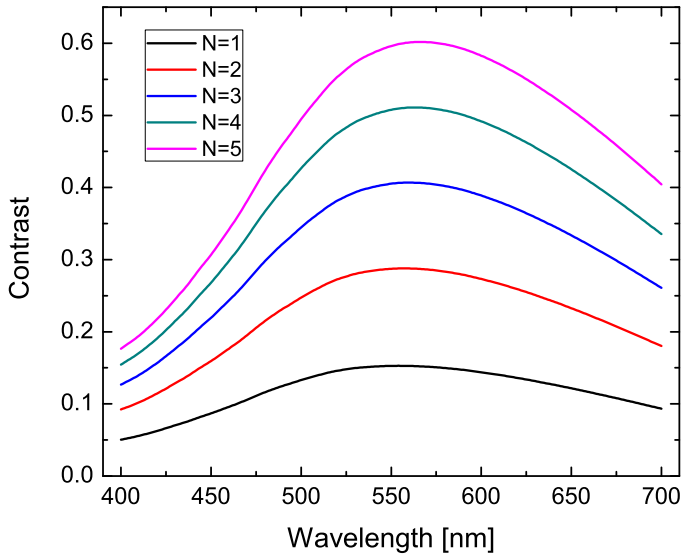

Figure 3.5: Optical contrast of graphene sheets with thickness ranging from one to five layers with an index of refraction $\tilde{n}_1 = 2.6 + 1.3i$ on 90nm SiO_2/Si.

We have also computed the contrast of multilayer graphene which consists of N monolayers. The thickness is then assumed to be N $\times$ 0.34nm. Each layer is found to absorb a portion of incident light [58] and thus the contrast increases with the number of layers as shown in Fig. 3.5. Therefore, graphene becomes more opaque with the number of layers as imaged in Fig. 2.3.

3.3.2 Contrast of Graphene at Oblique Incidence

While previous studies have mainly focused on the contrast at normal incidence, we show here the results as a function of incident angle for different polarizations in which the SiO_2 thickness is fixed at 90nm. Fig. 3.6 shows the evolution of the contrast as function of angle and wavelength in the visible spectrum for two polarizations. While no contrast enhancement is obtained for TM polarizations, TE polarizations show an improvement in the green wavelength as well as a substantial enhancement in the

blue wavelength. This observation seems to be different from the predicted decrease for circular polarization[49].

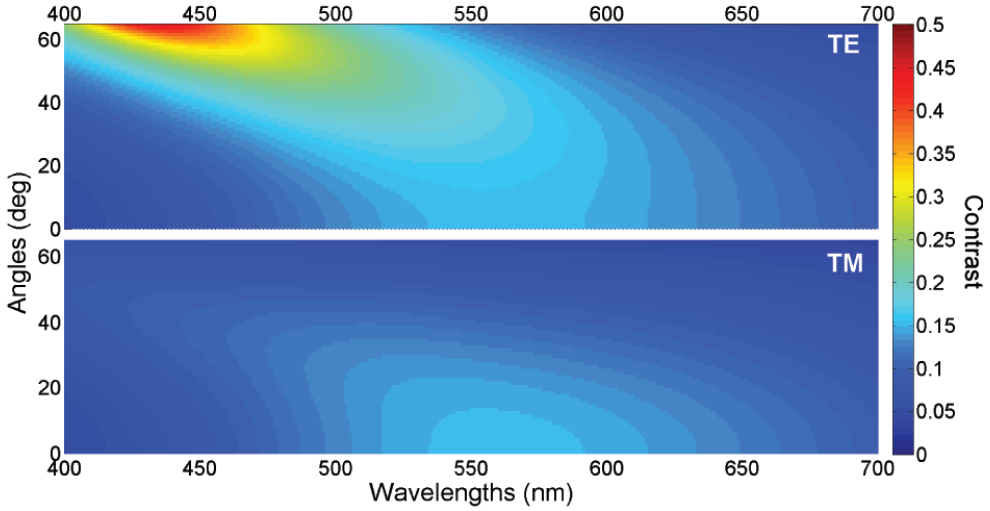

Figure 3.6: Contrast plot for TE and TM polarizations as a function of wavelength and angles for 90nm SiO_2/Si substrate. The expected contrast is shown on the color scale found on the right.

3.3.3 Experimental Procedure and Results

When observing graphene under an inspection microscope, the sample is perpendicular to the objective lens and is illuminated by the internal microscope light. In order to reproduce the behaviour predicted in Fig. 3.6, we designed a setup which orients the light's incident angle while using the microscope as a fixed detector. This was realized by building a moving stage (Fig. 3.7) to allow the sample to tilt.

The substrate is placed onto the stage underneath the objective lens and we locate the graphene flakes of interest at normal incidence. Once identified, the stage is then tilted by a screw and placed at the desired angle θ, while keeping the sample in focus. A white light source is shined onto the sample at 2θ relative to the objective lens. A polarizer is then placed in front of the light source and the signal is recorded onto the camera for both TE and TM polarizations. This process is repeated until all possible angles within experimental limits are covered. Due to obstacles between the external light source and sample, we can only acquire data between 23° and 65°. The error on

the angle is within 2°.

Figure 3.7: Experimental setup for angle detection measurements. The dashed circle is the substrate lying on the tilted stage and the stage's angle is adjusted with the screw.

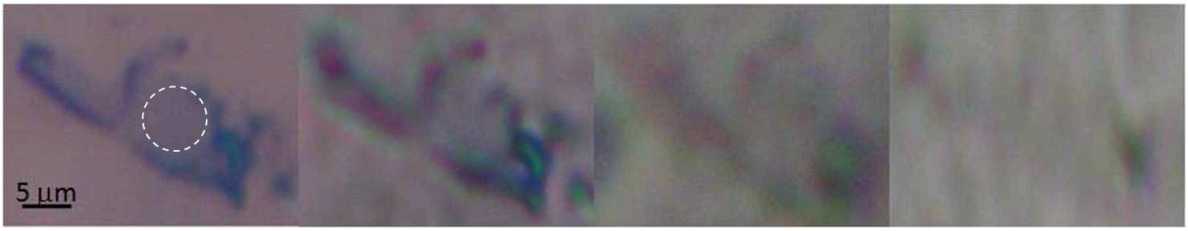

Figure 3.8: Thin graphene flakes on 90nm SiO_2 imaged on an optical microscope under TM polarizations. From left to right, each image is taken at 0°, 23°, 55° and 65° respectively. The dotted circle is the spot used for the contrast measured for a monolayer.

Fig. 3.8 are images of a single layer graphene surrounded by small fragments of few layered graphene on 90nm SiO_2/Si taken under TM polarizations. The first image is a typical image of a graphene monolayer at normal incidence. By increasing this angle, corresponding to images from left to right, the colors of the SiO_2 and graphene change. We notice that the SiO_2 layer goes from the colour purple to grey and the graphene monolayer tends to fade at 65°, and the few layered ones are barely visible.

Using an unfiltered light source, this decrease in contrast is valid for all wavelengths in the visible range as predicted in Fig. 3.6. The reverse effect is expected for TE polarization.

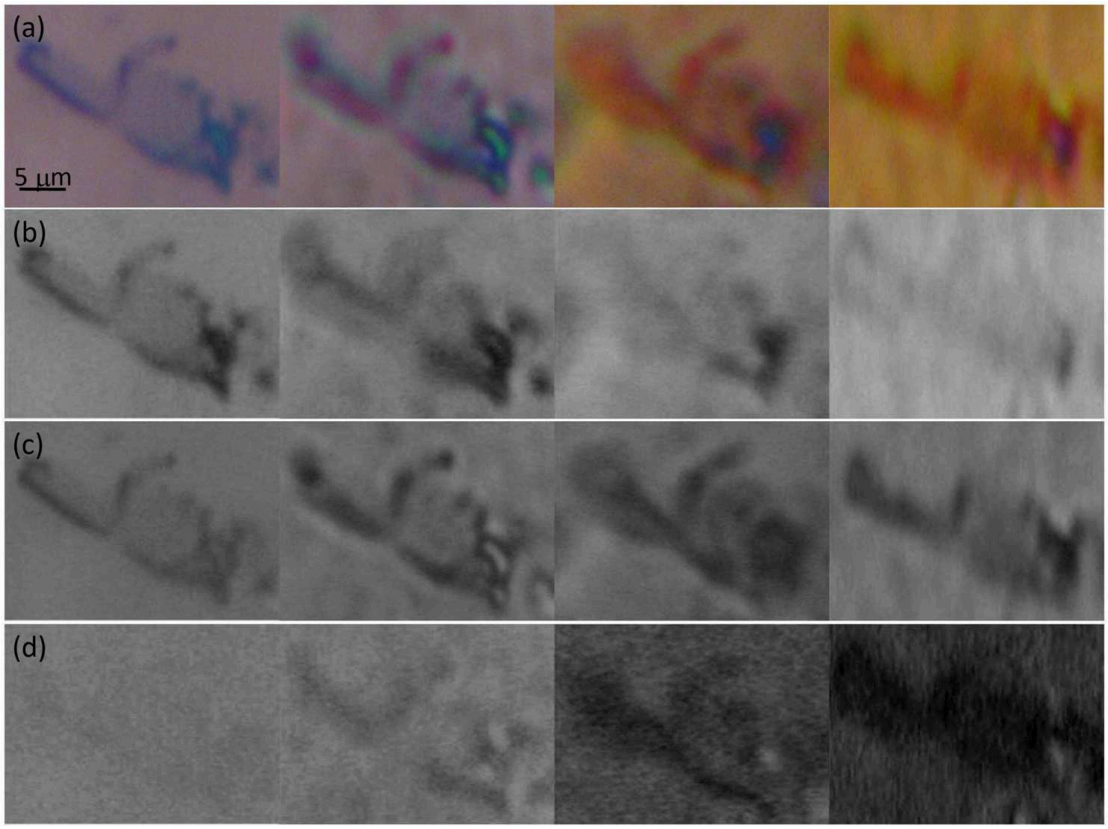

Figure 3.9: (a) Same graphene flakes as in Fig. 3.8 imaged under TE polarizations. (b) Red, (c) green and (d) blue images were obtained by selecting the corresponding wavelengths. From left to right, each image is taken at 0°, 23°, 55° and 65° respectively.

With TE polarization, Fig. 3.9(a) shows a change in color with increased angle and the graphene monolayer is still visible. However, the images do not provide any information about the contrast. To analyse the contrast, we selected the red, green, and blue wavelengths, respectively [Fig. 3.9(b)-(d)]. A decrease in contrast is seen in the red as the angle increases, while the contrast for green and blue increases. The procedure to compute the contrast is provided in the following section.

3.3.4 Contrast Measurements

The recorded images taken by the camera are in full colour. Each image, processed by Matlab, is divided into an array of pixels. Each pixel provides three specific values, one each for red, green and blue components. These values range between 0 and 255. The color of the pixel is then determined by the combination of red, green and blue intensities. For instance, a typical intensity profile is shown in Fig. 3.10 for red, green and blue. The plot displays two distinct steps in the red and green spectra which correspond to the graphene and the substrate. In blue wavelength, no steps are easily observed, meaning that the graphene flake is nearly invisible as seen in the first image of Fig. 3.9(d). The contrast is then calculated as the difference of the measured intensity from substrate and graphene respectively, and normalize with respect to the substrate. This provide a direct measurement for the red, green and blue reflection contrast $C_{\{R,G,B\}}$ and Eq.3.32 can be rewritten as

$$C_{\{R,G,B\}} = \frac{I_{substrate\{R,G,B\}} - I_{graphene\{R,G,B\}}}{I_{substrate\{R,G,B\}}}. \tag{3.33}$$

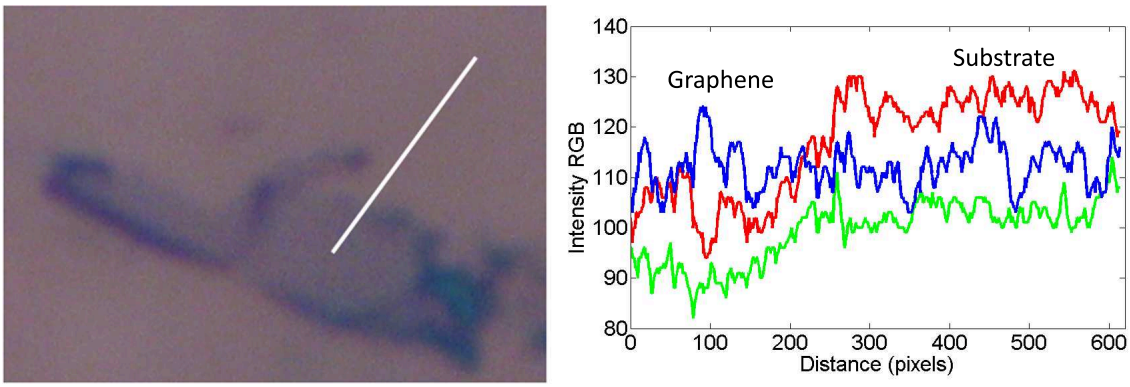

Figure 3.10: Left: Image of graphene at normal incidence. White line is the measurement line starting from the graphene to the substrate. Right: Plot of the red, green and blue intensity profiles.

Large errors are seen in the intensity profiles of Fig. 3.10. These may originate from electrical noise from the camera, variations on the sample, particles trapped inside the microscope's optical system and external light source. While these effects cannot be ignored, it is best to reduce these fluctuations. This is achieved by selecting

a set of pixels on the graphene as well as on the substrate and average their respective intensities. In addition, the data were taken three times on different graphene monolayer samples to ensure that a clear relationship between the contrast and the angle of incidence is observed. We then compare the calculated contrast with the measured data for different wavelengths in Fig. 3.11. The data follows the calculated one within the error bars obtained from the sample to sample standard deviation. We measured that the contrast is enhanced up to 50% at 65 degrees and this should be compared to a maximum contrast of 15% when the light is normally incident.

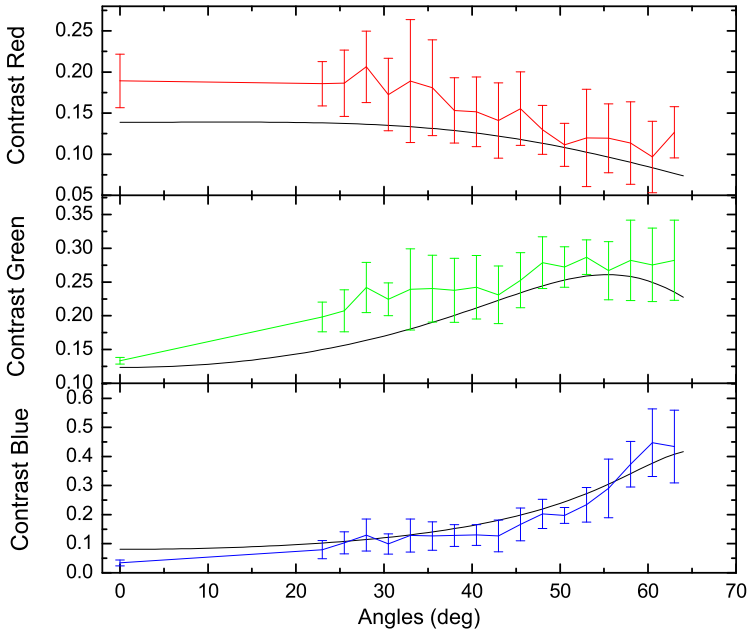

Figure 3.11: Comparison of experimental (color curves) and calculated (black curves) contrast plot as a function of angle at a fixed wavelength. (a) Red contrast plot at a wavelength of 620nm (b) Green contrast plot at 495nm. (c) Blue contrast plot at 450nm. The error bars are the standard deviations for 3 different data sets and the lines are guides to the eye.

We noticed that the measured contrast does not exactly overlap with the calculated data. This deviation has also been observed at normal incidence in Ref. [28]. This can be attributed to the finite aperture of the objective lens. Depending on the numerical aperture, a small range of the light's incident angle also contribute to the measured

contrast[57]. Another explanation is the use of the index of refraction of graphene. While this value is assumed to be the same as graphite, the absorption of graphene may differ from the one of graphite. Currently, no concensus has been reached on its value since its exact value likely depends on substrate properties such as doping.

3.4 Graphene on Multilayered $GaAs/Al_{0.3}Ga_{0.7}As$

Based on our understanding of the contrast of graphene on SiO_2, we now turn to the possibility of enhancing the contrast of graphene on other substrates, which would offer a smoother and cleaner electrical surface. Here, we have at our disposal a conventional $GaAs/Al_{0.3}Ga_{0.7}As$ heterostructure with a two-dimensional electron gas at the interface. The substrate consists of a 8-layer Fabry-Pérot structure with graphene on top as depicted in Fig. 3.12. This structure can be used as a FET device which mimics devices of SiO_2/Si. The cap layer (the undoped-GaAs) can be employed as an insulator and the 2DEG, as a back gate. Normally, graphene is invisible on GaAs due to its low contrast, preventing its use as a substrate. It was previously reported that its contrast is -0.0059 for a homostructure of GaAs (Table 1.1) at normal incidence[31]. For our heterostructure, the intensity of the reflected waves is calculated by considering 9 layers, leading to 8 transfer matrices in Eq.3.27. The index of refraction parameters are obtained from Ref.[54]. At normal incidence, a contrast of 2% for a single layer graphene was obtained, which improves the contrast by almost a factor of 4 compared with a monostructure.

Fig. 3.13 shows the evolution of contrast as a function of angle for a 4-layer graphene on the GaAs/AlGaAs heterostructure for both TE and TM polarizations. It is interesting to note that the contrast enhancement only occurs for TM polarization as opposed to TE polarization in the SiO_2 case. A contrast shift occurs with the number of graphene layers, which allows us to identify the number of layers as four.

Fig. 3.14(a) illustrates the contrast evolution of a few-layer graphene on GaAs under TE polarization. The visibility of graphene decreases at higher angles for all wavelengths. This behaviour is expected for TE polarization. In contrast to TM polari-

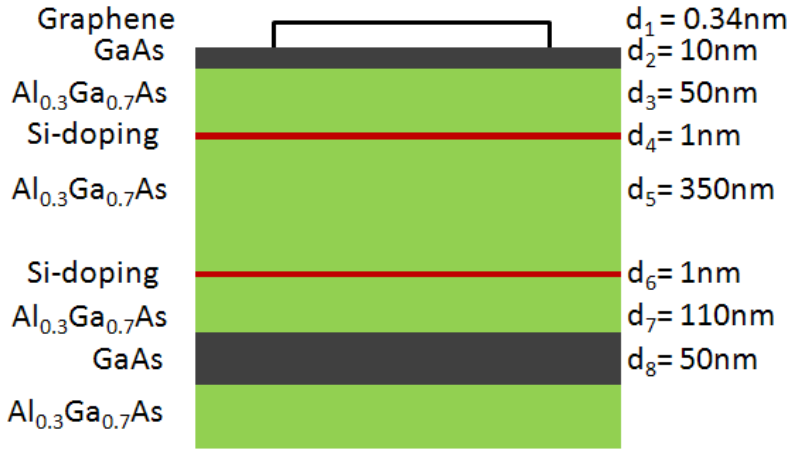

Figure 3.12: Schematic of graphene on a 8-layer GaAs/AlGaAs heterostructure.

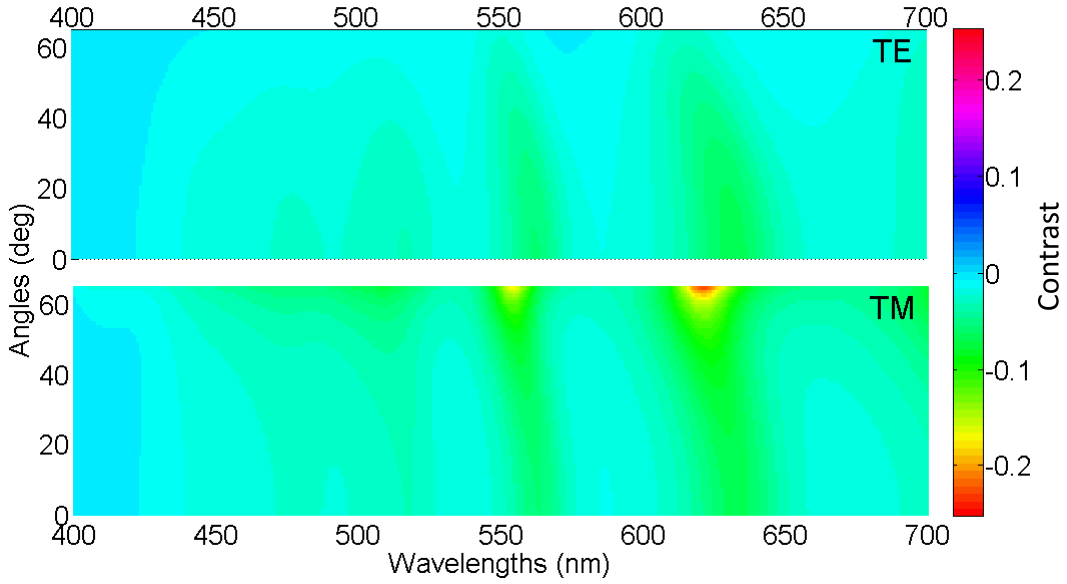

Figure 3.13: Contrast plot for a 4-layer graphene flake as a function of angle and wavelength on a 8-layer GaAs/$Al_{0.3}Ga_{0.7}As$ heterostructure under TE and TM polarizations.

zation (Fig. 3.14(b)), the graphene flake of interest becomes brighter with increased angle for red and green (Fig. 3.14(c) and (d) respectively). For blue (Fig. 3.14(e)), it is barely observed.

We now compare the calculated contrast with the data obtained in Fig. 3.15. The error bars are obtained from the standard deviation of two different data sets. For

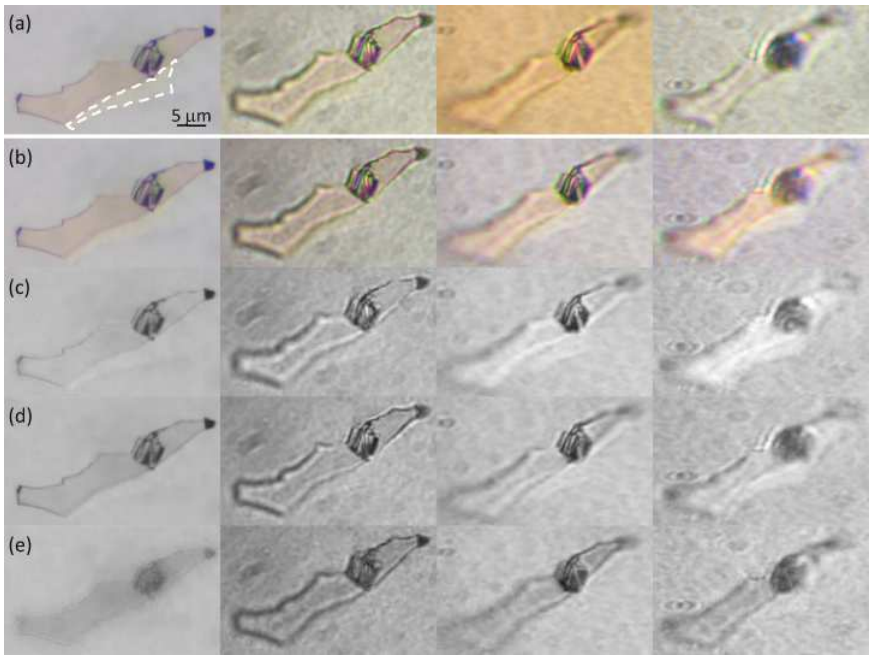

Figure 3.14: Graphene flakes on GaAs imaged under (a) TE and (b) TM polarization. (c) Red, (d) green, and (e) blue images were obtained by selecting the corresponding wavelengths. Each column represents images taken at 0°, 23°, 55° and 65° respectively. The area delimited by the dashed line is the area used for the contrast measurements of a few layer graphene.

green and blue, large fluctuations at small angles are observed. This is due to the low contrast of the graphene flake leading to an increase in the importance of noise. The measurements demonstrate that a contrast of about 12% can be reached when tilted at 65 degrees under TM polarization. Overall, the contrast increases with angle.

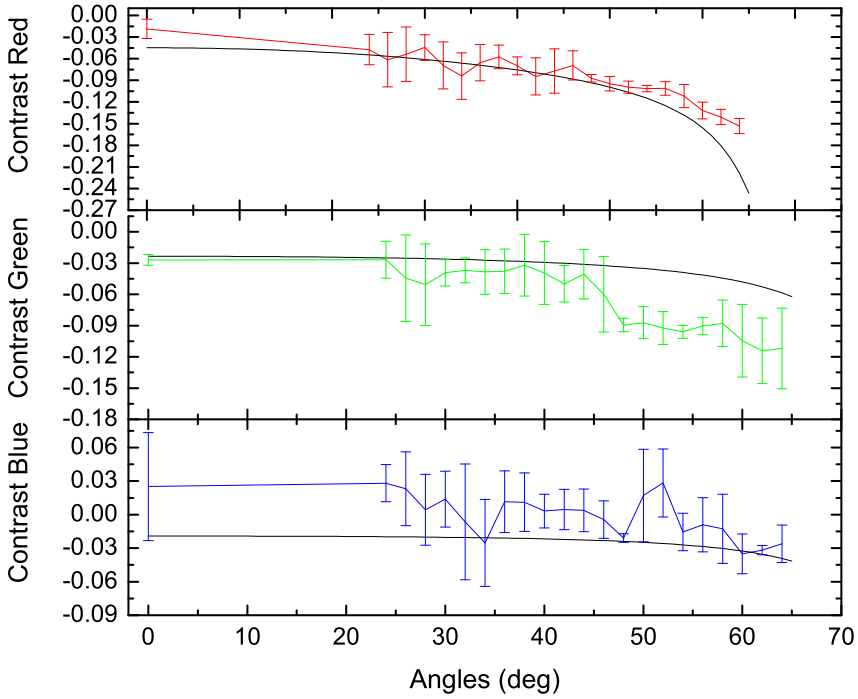

Figure 3.15: Comparison of experimental (color curves) and calculated (black curves) contrast plot as a function of angle at a fixed wavelength. (a) Red contrast plot at a wavelength of 620nm. (b) Green contrast plot at 495 nm. (c) Blue contrast plot at 450nm.

4

Graphene Synthesis by Chemical Vapour Deposition

So far, graphene has mostly been produced via mechanical exfoliation of highly oriented pyrolytic graphite (HOPG). While these micron-size films are suitable for studying fundamental science, it is difficult to scale to the large areas necessary for potential applications. Alternatively, chemical vapour deposition (CVD) on single-crystal transition metals has shown full coverage of high quality graphene, but the expensive cost of single crystal substrates is a limiting factor[59, 60]. Recently, more affordable polycrystalline materials such as nickel films[22, 61] and copper foils[21, 62] have been successfully used as substrates to produce large high quality graphene films by CVD. Despite these recent achievements, very little is understood about the initial nucleation stage of graphene and the growth kinetics.

This chapter focuses on the synthesis of graphene on copper foils. This synthesis is realized from a mixture of methane and hydrogen following a similar procedure provided by Li *et al.*[21]. We will first compare the growth mechanisms of graphene on copper (Cu) and nickel (Ni). Afterwards, the CVD setup and sample preparation will be presented. This will be followed by a discussion of our preliminary results on a few growth parameters that influence the morphology of graphene. Finally, transfer techniques from metallic to insulating substrates will be described.

4.1 Growth Mechanism on Nickel and Copper

The possibility of synthesizing large-scale graphene is not at all surprising considering the success of growing carbon nanotube. It was mostly a matter of finding the

appropriate catalysts and right precursors for large-scale growth of graphene. The quality of CVD-grown graphene varies depending on the substrate used. The highest quality graphene is grown on Ni and Cu foils, but its quality cannot yet be compared to that of mechanically exfoliated graphene. Cu and Ni catalysts do not provide the same final results, suggesting that the graphene is synthesized differently depending on the metal employed. The growth mechanism of both catalysts is summarized in Table 4.1.

Table 4.1: Summary of the growth mechanism of graphene on Ni and Cu.

Catalysts	Copper	Nickel
Carbon Solubility	Negligeable	High
Growth Mechanism	Surface-catalysed	Segregation and Precipitation
Cooling	Independent	Critical
Number of Graphene Layers	Mainly Single Layers	Few to Several Layers

On Ni, graphene production results in multilayered and non-uniform films. This is attributed to the high carbon solubility in Ni. The growth process is depicted in Fig. 4.1(a). At high temperature, hydrocarbons decompose at the surface of the Ni foil and carbon atoms then diffuse into the metal. Finally, the cooling process is the most critical step that determine the quality of the graphene films. For fast cooling rates (quenching), carbon atoms do not have enough kinetic energy to form graphene and a poor crystalline and defective structure on the surface of Ni results. For moderate cooling rates (about 10°C/s), carbon atoms outdiffuse onto the surface and form graphene. For slow cooling rates, carbon atoms have time to diffuse into the bulk and only a small amount segregates[63]. This gives an insight on the growth mechanism of graphene on Ni in the CVD process, but a precise control on the number of layers seems to be a challenging task.

As for Cu, large films are dominated by graphene monolayers and this is due to the very low carbon solubility in Cu. It was shown that the growth is a surface-catalysed process and self-limiting. This means that once the surface of Cu is fully covered with graphene, the process is terminated as sketched in Fig. 4.1(b). In addition, the

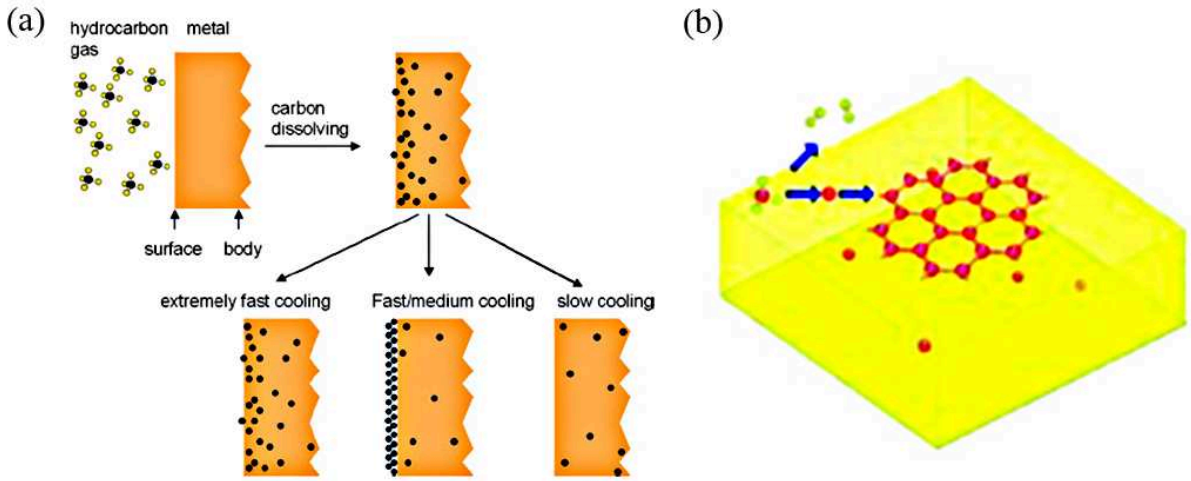

Figure 4.1: Illustration of the (a) carbon segregation process for Ni and (b) surface catalysed for Cu. Reproduced from [63] and [64].

second layer of graphene is difficult to grow at large-scale as it requires a contact to the catalyst.

4.2 CVD Setup

Synthesis of graphene is realized at low pressure by thermal CVD. A typical CVD system consists of three main components: a furnace, a gas handling system and vacuum pump as shown in Fig. 4.2 and schematized in Fig. 4.3.

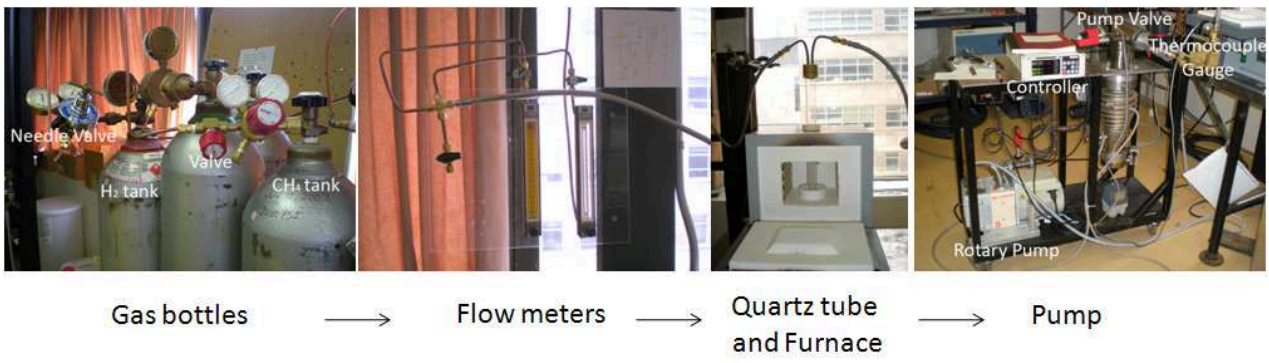

Figure 4.2: Pictures of our CVD setup.

The furnace is heated with resistance wires inside the chamber and its temperature is controlled by a programmable microcontroller. A vertical quartz tube with a

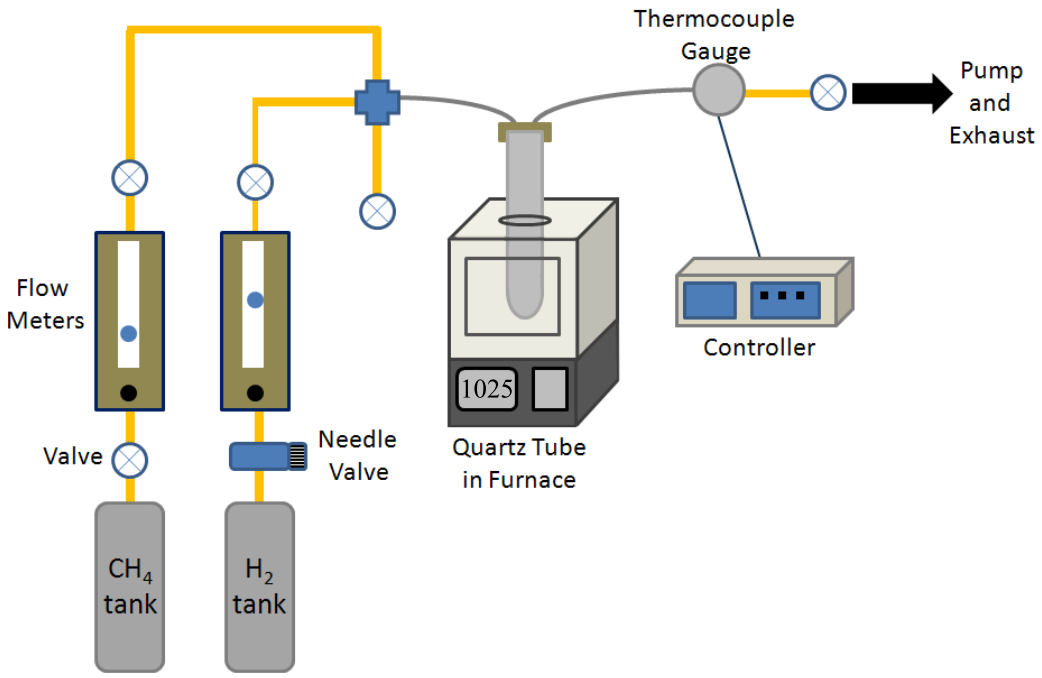

Figure 4.3: Schematic of the CVD setup of Fig. 4.2

diameter of one inch is inserted into the oven. The opening of the quartz tube is then closed with a brass plate and an o-ring is placed in-between to avoid any damages and leaks.

The inlet and outlet of the plate are connected with flexible stainless steel tubing to the gas and vacuum system respectively. These tubes are purposedly used to handle the quartz tube with ease when loading or removing the sample. The outlet of the plate is connected to a thermocouple gauge in which the pressure is measured by the controller. The whole system is pumped to a pressure of 10^{-4} Torr with a rotary pump and finally, pumped to the exhaust.

At the inlet of the tube, the gas system is made up of several gas lines that provide the oven with the desired gas mixture. Each gas line consists of a gas bottle equipped with a regulator to adjust the pressure of the gas. This is followed by a two-way valve allowing the opening and closing of the gas line without changing any parameters set by the regulator. The valves are then linked by 1/4-inch outer diameter copper tubes to the inlet of the flowmeters. The outlet is connected to a cross connector in which

the gas mixing proceeds. The extra port on the cross is connected to a valve which is used for venting the CVD system.

The two main gases used for graphene growth are hydrogen (H_2) and methane (CH_4). Each gas line consists of a valve and flow meter connected to each applied gas bottle and flow rate. For instance, the hydrogen gas line requires a flow rate of about 4 sccm (standard cubic centimeters per minute). Because standard valves are not sensitive to low flow rates, a needle valve is thus connected to precisely regulate this low flow. In addition, a sensitive variable area flow meter from Matheson (Model 601) is installed to read flow rates down to 1 sccm. The flow rate used for methane is higher than for hydrogen. Thus, any standard valve and flow meter (Model 602) which can output down to 10 sccm suffices.

4.3 Experimental Procedure

4.3.1 Cleaning Procedure

Before running the CVD system, a cleaning process is required to reduce the amount of contaminants on the quartz tube and the catalyst. From experience, after three runs of CVD growth with an uncleaned quartz tube, poor quality graphene is formed which usually does not reach full coverage. It seems that contaminated regions on the catalyst terminate the growth process as imaged in Fig. 4.4. To ensure optimal results, cleaning must be performed before each run.

The quartz tube is first cleaned in concentrated nitric acid to remove carbon and copper residues, followed by a cleaning in de-ionized (DI) water. Afterwards, the tube is baked in air at 1100°C for 15 minutes and then cooled down to room temperature before loading the sample.

Commercially available 25μm-thick Cu foil (Alfa Aesar, item No. 13382) is used as our catalyst. To remove contaminants such as packaging residues, oil and dust particles, the substrate is cleaned ultrasonically in acetone (10 s), acetic acid (10 mins), acetone (10 s), isopropanol alcohol (IPA) (10 s). Finally, the Cu foil is gently blown dry with a N_2 gun.

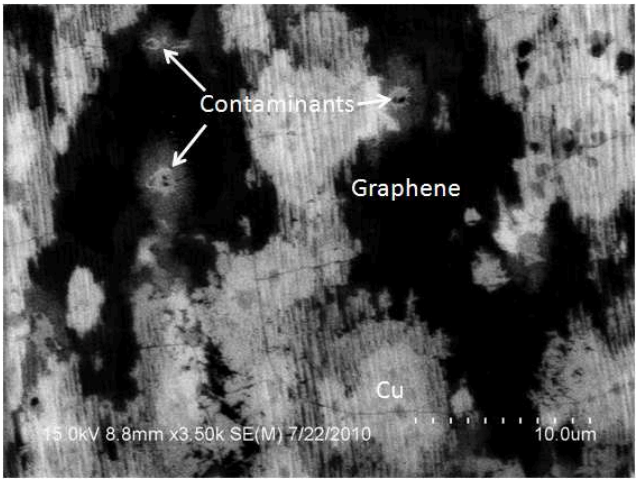

Figure 4.4: SEM image of graphene on Cu synthesized in uncleaned conditions.

4.3.2 *CVD Growth of Graphene*

A typical growth procedure conducted in our CVD system is shown in Fig. 4.5.

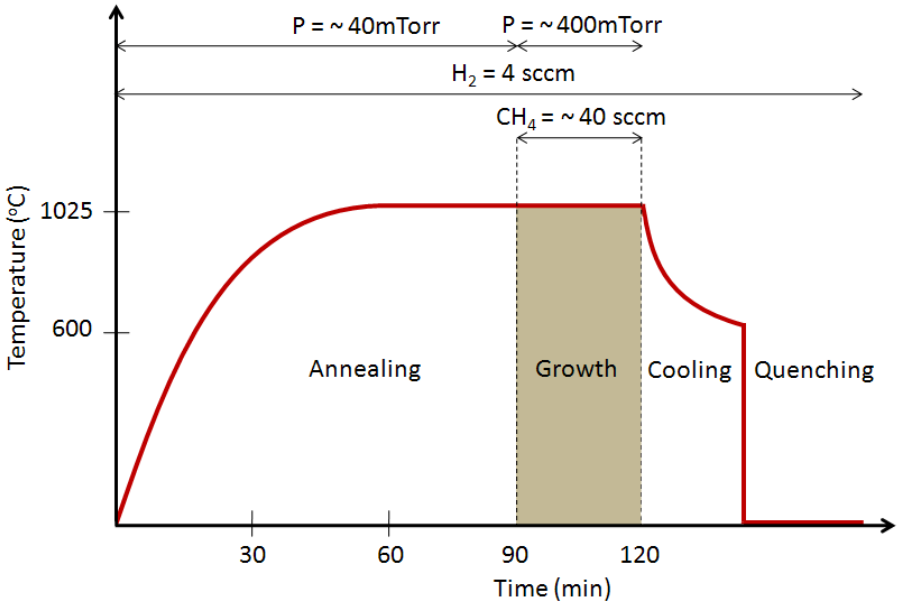

Figure 4.5: Plot of the growth parameters (temperature, pressure, precursor and flow rate) as a function of time.

First, a clean Cu foil is placed at the bottom of the quartz tube. The system is then pumped down to base pressure (10^{-4} Torr) with the rough pump. Once the pressure reaches the base level, the valves of both H_2 and CH_4 gas lines are opened

and the flow rate is adjusted with the control valve of the flow meter. The CH_4 valve is then closed, leaving the H_2 flow on. The pressure is then readjusted using the rough pump valve to about 40 mTorr. Afterwards, the furnace is heated up to the desired temperature, up to 1025°C. The temperature is stabilized for 30 mins in H_2 to prevent forming oxides on the Cu during growth. The CH_4 valve is opened to initiate the graphene growth and the pressure is readjusted to 400mTorr. Once the duration for the growth has elapsed, the CH_4 valve is closed and the furnace is cooled to room temperature. Since the cooling rate is not a critical factor, the quartz tube is safely removed from the furnace at 600°C and quenched in cold water. The gas lines and the roughing pump valve are then closed and the valve at the cross is opened for venting. The sample is removed from the quartz tube. Fig. 4.6 shows the Cu foil covered with the graphene film, resulting in a shinier surface than bare Cu foil.

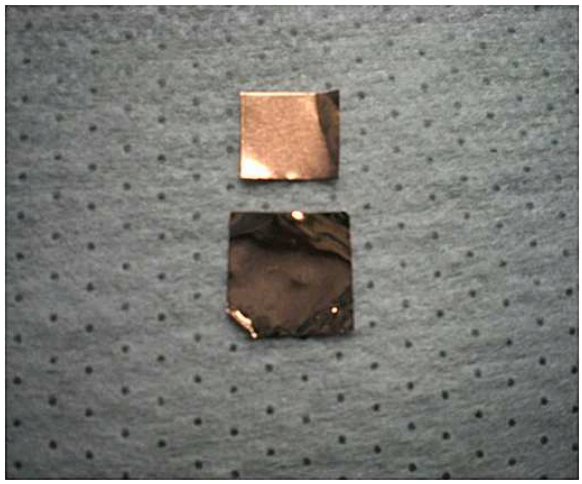

Figure 4.6: Picture of bare Cu foil (top) and graphene-covered Cu foil (bottom).

4.4 Methodology

Most reported CVD setups synthesize graphene in a horizontal quartz tube. However, our setup, which consists of a vertical tube, still provides high quality graphene, no noticeable difference in the results has been observed. Optimal quality and coverage of graphene varies from one CVD system to another. One needs to consider the

following growth parameters that contribute to the CVD process:

- Precursor used
- Gas flow rate
- Growth temperature
- Pressure before, during and after the growth
- Duration of the growth
- Catalyst used (foils or e-beam evaporated)
- Catalyst thickness

Details on the growth mechanism due to the influence of the growth parameters are still under active development. We will discuss in the following sections some of our preliminary results of CVD growths. We will focus on the effects of growth temperature and duration, and hydrogen gas flow rate. The samples are characterized via Raman spectroscopy and SEM. The data acquisition for Raman spectroscopy was performed using the same settings mentioned in Section 2.1.4.

4.4.1 Effect of Growth Temperature

Temperature is a critical factor in the synthesis of graphene because sufficient energy is required to dissociate the hydrocarbon precursor such that reactions with the catalysts occur. Fig. 4.7 illustrates the temperature effect on the synthesis of graphene while holding the growth duration at 30 minutes. These SEM images show that the density and size of growth domains increase with temperature. These suggest that a significant amount of carbon atoms contributes in the formation and growth of nucleation sites resulting in faster growth at higher temperatures. We also notice that a faster growth occurs depending on the crystal orientation of the Cu grain as shown in Fig. 4.7(a). This behaviour was observed consistently and indicates the preferred Cu orientation for the growth of graphene.

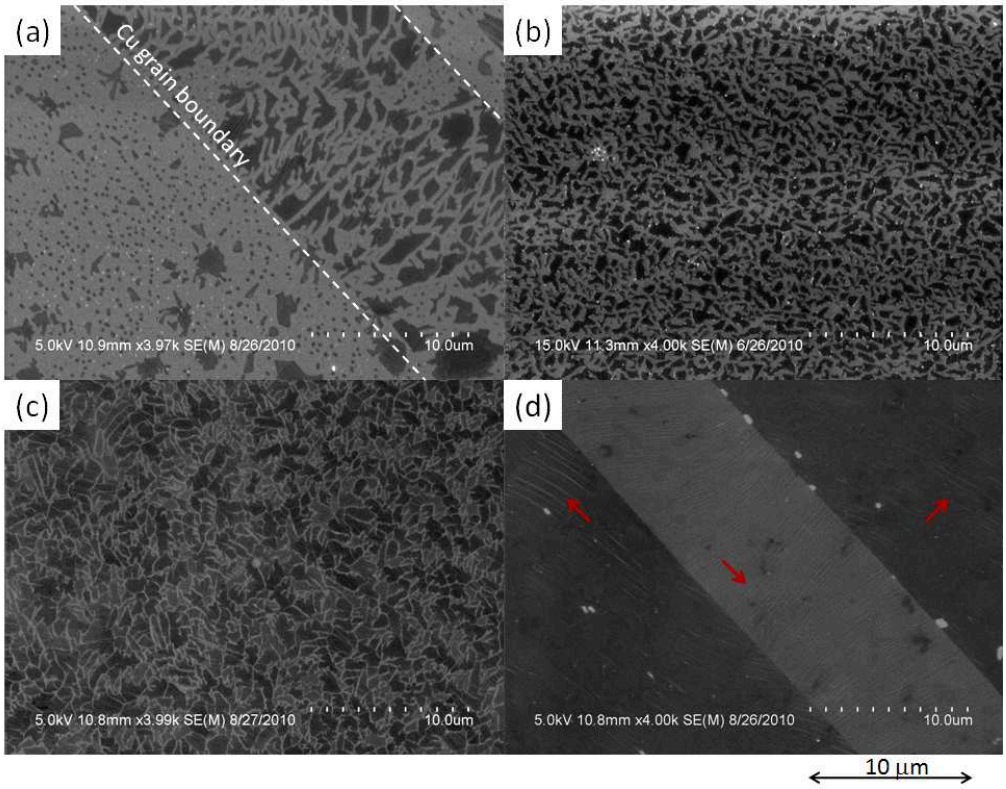

Figure 4.7: SEM images of graphene on Cu grown for 30 minutes with different growth temperature: (a) 900°C, (b) 950°C (c) 975°C, and (d) 1050°C respectively. Red arrows indicate graphene ripples on the Cu grains.

We investigated the Raman spectroscopy for each growth temperature between 900°C and 1075°C. The large intensity ratio of the 2D (∼2700 cm^{-1}) over G (∼1580 cm^{-1}) peak is associated to a graphene monolayer and the key results are found around 2700 cm^{-1} as shown in Fig. 4.8(a). The Raman spectra were measured at 10 different spots of the sample to ensure that a clear relationship between the position of the 2D peak and growth temperature is observed. The error bars are the standard deviations of these data sets as plotted in Fig. 4.8(b). We noticed that the 2D peak is blueshifted with increasing growth temperature while shifts do not occur on the G peak. We claim that this behaviour is a result of uniform biaxial strain due to compression of Cu during the cooling process which causes stress on the graphene. This claim is based on results reported by Novoselov *et al.* where uniaxial strain is applied on exfoliated graphene[65, 66]. Tension and compression induce a shift

in the 2D peak and also, the G peak splits into 2 peaks in response of the distorted hexagonal lattice. The latter represents the two possible phonon modes of the in-plane bond-stretching of a pair of carbon atoms.

We simulate the behaviour of free-standing graphene due to isotropic tension and compression. This is realized by choosing values of the carbon-carbon bond length out of its equilibrium value a_0 (= 1.42Å). We know that compression ($< a_0$) induces an enlargement of the Brillouin zone as well as a narrowing of the cone in the linear dispersion resulting in a decrease of the Fermi velocity. With this argument, the double-resonance process (Section 2.1.4) is employed to explain the induced shift in the 2D peak. Fig. 4.9 illustrates the Raman process of compressed graphene and compare it to unstrained graphene. The 2D peak arises through emission of two phonons with frequency of $\mathbf{q}_0$ for unstrained graphene. Under compression, the phonon's frequency increases to $\mathbf{q}^*$ and thus, a shift to a higher frequency is expected for the 2D peak, consistent with the trend in Fig. 4.8(b). As for the G peak, the hexagonal structure is kept intact under uniform biaxial strain. Therefore, a shift or splitting of the G peak should not occur.

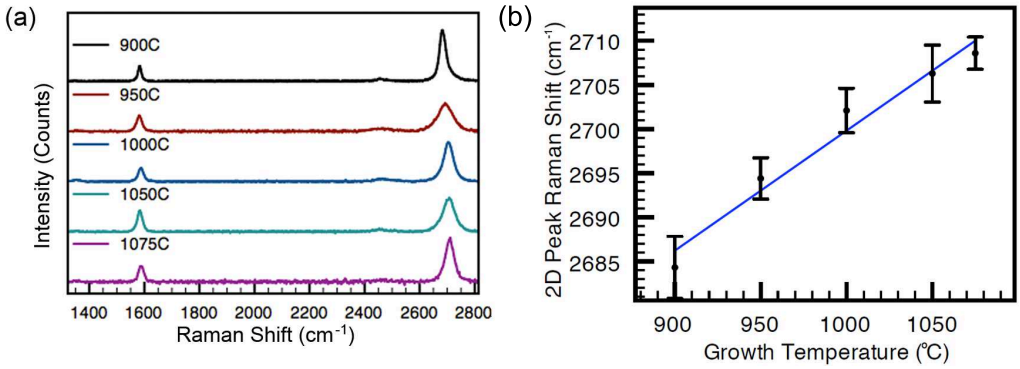

Figure 4.8: (a) Raman spectra for each growth temperature. (b) Average position of the 2D peak for different growth temperatures. The error bars are the standard deviations for 10 different data sets and the line is a guide to the eye.

For unstrained graphene, the position of the 2D peak is located at 2680 cm^{-1}. In our data, the 2D peaks are higher than the one of unstrained positions. Clearly, compressive strain is present at any given temperature. The error bars can then be

represented as an average strain induced on the graphene sample. We notice two regimes in Fig. 4.8(b). For temperatures lower than 1000°C, a large increase in the Raman shifts is observed with increasing growth temperature. We think that the graphene film is held to the Cu substrate by Van der Waals forces while it is in a compressed state. For temperatures exceeding 1000°C, the data points are less spaced. This seems to suggest that the graphene gradually detaches from the substrate to compensate for the large amount of compressive strain. This detachment could explain the formation of ripples imaged in Fig. 4.7(d). Therefore, our results illustrate that the graphene islands can form at any growth temperature exceeding 900°C, despite the lattice mismatch of 3.9% between graphene and Cu[67, 68].

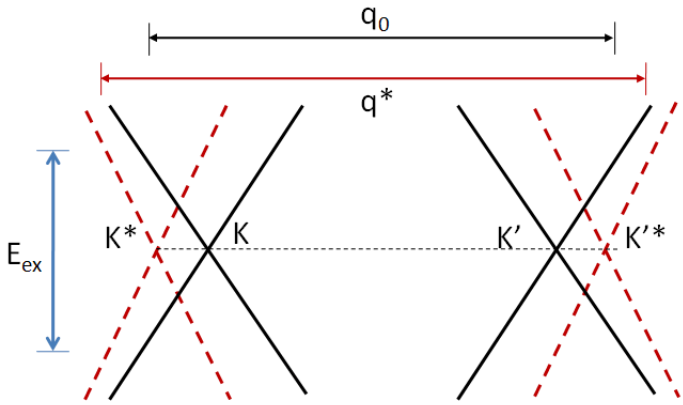

Figure 4.9: Schematic diagram showing the electronic structure of compressed graphene monolayer (red dash lines) as well as unstrained graphene (black lines). Black and red arrows indicate the emitted phonons from the double-resonance process

4.4.2 *Effect of Growth Duration*

Under prevailing conditions indicated in Table 4.2, it was found that the growth of graphene is a quick process. Fig. 4.10 shows the evolution of graphene growth with time duration ranging from 2 minutes to 15 minutes at 1025°C. It seems that most of the growth domains have coalesced to form graphene in 5 minutes but large density of bright spots, showing the uncovered Cu, are still observed. When growth duration is increased to 10 mins, very few bright spots are left. This seems to suggest that carbon atoms actively move in and out of the edges of the growth domains until all the

domains are linked, forming a solid and stable graphene sheet. After 15 minutes, full coverage is achieved; longer growth times yield similar results. Therefore, we have not observed the formation of multi-layer graphene sheets for longer times, demonstrating the self-limiting growth process of Cu.

Table 4.2: Parameters for different growth time.

Time (mins)	Temperature (°C)	Pressure (mTorr)	H_2 (sccm)	CH_4 (sccm)
2	1025	410	4	40
5	1025	400	4	41
10	1025	410	4	37
15	1025	510	4	37

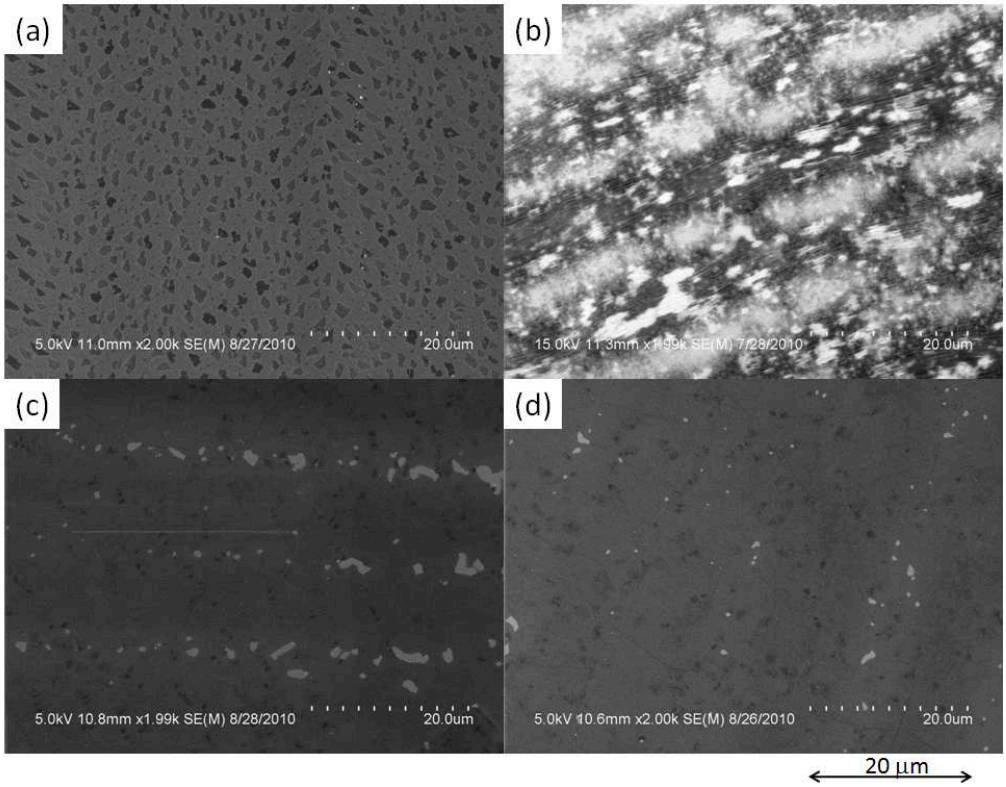

Figure 4.10: SEM images of graphene on Cu with different growth times: (a) 2 mins, (b) 5 mins (c) 10 mins, and (d) 15 mins. Dark regions shows the graphene coverage and bright spots are the regions not covered by the graphene.

4.4.3 Effect of Low Hydrogen Flow Rate

To observe the effect of H_2, we have used a flow rate of about 1.5 sccm instead of the original 4 sccm. The growth conditions are indicated in Table 4.3.

Table 4.3: Parameters for growth at lower H_2 flow.

Sample ID	Time (mins)	Temperature (°C)	Pressure (mTorr)	H_2 (sccm)	CH_4 (sccm)
C3	30	1000	400	1.5	35

H_2 is employed to prevent the Cu from oxidizing due to oxygen impurities found in CH_4[21]. It appears that cracks in the graphene layer arise from a lack of hydrogen as shown in Fig. 4.11. One can quantify the density of defects by taking the ratio of the D over G peak (I_D/I_G)[69]. From the Raman spectrum, the obtained value is about 1/3, indicating that a fair amount of defects is found in the graphene. A possible explanation is that the H_2 selectively etches amorphous carbon at the graphene edges and serves as a secondary nuclei to coalesce the graphene islands[70]. A surplus of hydrogen, not shown here, leads to a dominant etching effect, preventing the synthesis of graphene[71].

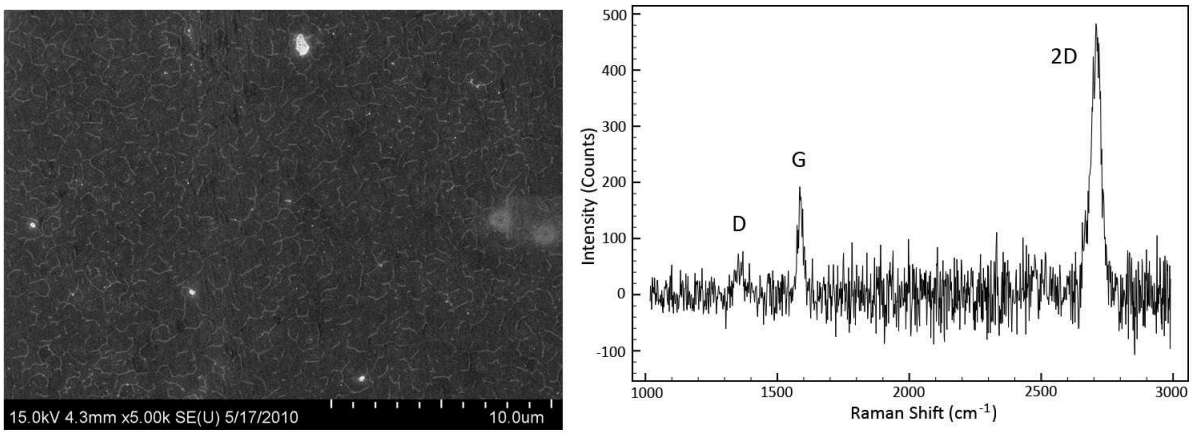

Figure 4.11: SEM image and Raman spectrum of graphene grown at low hydrogen flow rate.

4.5 Graphene Transfer on Non-Metallic Substrates

Graphene on metallic substrates is not that interesting considering that most applications require graphene to be on an insulating substrate. It is thus necessary to develop methods to transfer graphene sheets on a variety of substrates while allowing efficient detection once placed on the substrates. Only a few transfer techniques are known to give fairly good results, but large-scale defect-free transfer is not yet perfected and tends to leave traces of chemical residues behind.

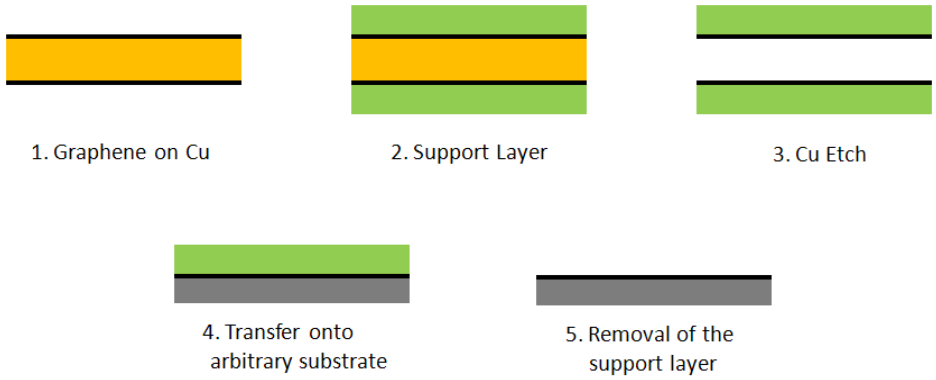

Figure 4.12: Schematic of a typical deposition of graphene on substrates.

A schematic of a typical transfer process is shown in Fig. 4.12. Graphene cannot remain free-standing without any supporting layer, or it will curl up. Here we use either PMMA or Nitto Denko thermal release tape (3195MS) as a supporting layer. Graphene grows on both sides of the Cu, but we place the supporting layer only on one side, then the Cu film is stripped off in an oxidizing solution of 0.1M ammonium persulfate ($(NH_4)_2S_2O_8$). Ferric chloride ($FeCl_3$) is also suggested as an oxidizing agent[72], but tends to leave traces of cupric oxide on the graphene. The last step is to transfer the support/graphene onto a substrate and then remove the supporting layer.

Fig. 4.13(a) shows a picture of a synthesized cm^2-sized graphene transferred by thermal release tape on a SiO_2/Si wafer. This tape can be used to easily manipulate the graphene film and position on a target location of the substrate. This supporting layer is removed by heating to 120°C so that it loses adhesion. Fig. 4.13(b) is an

optical image of the graphene film and observed tape residues on the surface of the graphene film. These can be removed by annealing or in solvents. Fig. 4.13(c) shows a close-up of the graphene flake using SEM. The appearance of cracks on the graphene film might originates from the pressure applied to adhere the tape onto the substrate or graphene that did not make contact with the tape, thereby causing teared regions. Fig. 4.13(d) shows a representative Raman spectrum which is associated to a single layer graphene and the intensity ratio I_D/I_G indicates the density of defects in the graphene is small. We also notice some dark spots on the graphene film which might be bilayer graphene but no specific investigation of these spots has been performed.

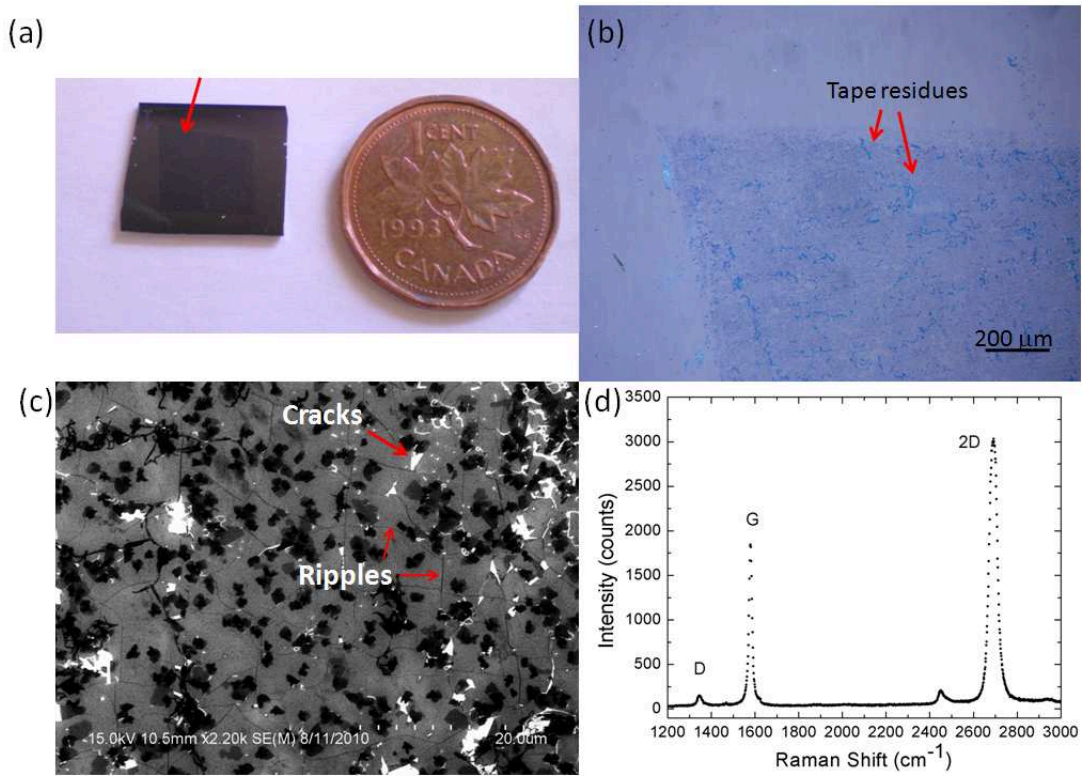

Figure 4.13: (a) Picture of a cm^2 CVD graphene film on SiO_2/Si wafer transferred using thermal release tape. Arrow indicates the edge of graphene. (b) Optical image of the graphene film with traces of tape residues. (c) SEM image showing cracks and ripples. (d) Raman spectrum of CVD graphene on SiO_2/Si.

Fig. 4.14(a) shows a picture of graphene transferred using PMMA onto a SiO_2/Si wafer. For this sample, $FeCl_3$ was employed to etch the Cu foil and the graphene/PMMA is scooped out of the solution with a substrate. PMMA is then dissolved carefully

with a slow acetone flow. The resulting graphene is shown in Fig. 4.14(b) in which we observe traces of copper left by the $FeCl_3$ solution and folded graphene from the transfer. One would notice that the colour of the graphene film is bluish compared to other graphene flakes on SiO_2 which are dark purple such as Fig. 4.13(b). This suggests that a thin layer of PMMA still remains on the graphene even after cleaning with acetone. We found that the the entire film was transferred and no cracks were observed as shown in Fig. 4.14(c), unlike Li *et al.* who claim to have observed micron-sized cracks due to their transfer[72]. The gray regions represents the graphene and the black islands might be copper residues but we have not investigated these spots in great details. Our Raman spectrum in Fig. 4.14(d) indicates that the film is a graphene monolayer and the defect density is relatively low.

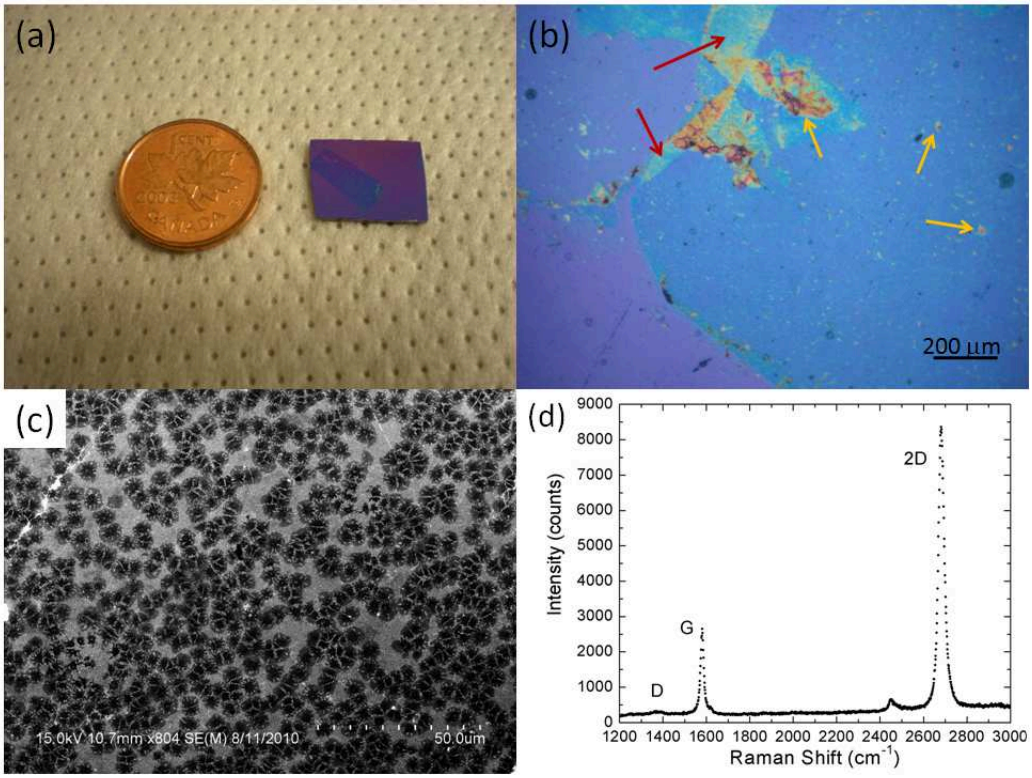

Figure 4.14: (a) Picture of a cm^2 CVD graphene film on SiO_2/Si wafer transferred by PMMA. (b) Optical image of the graphene film with Cu residues from $FeCl_3$ solution indicated with yellow arrows. Red arrows indicate folded regions of graphene due to transfer. (c) SEM image showing barely no cracks. (d) Raman spectrum of CVD graphene on SiO_2/Si.

4.5.1 Preliminary Transport Measurements

The sheet resistance is a good indication of the electrical quality of the sample. A four-terminal configuration, known as the van der Pauw technique, is employed to measure the resistance of the sample. CVD-grown graphene sheets were transferred via PMMA on glass and on SiO_2/Si wafer. Small droplets of SPI conductive silver paint were then placed on the periphery of the graphene film as shown in Fig. 4.15 and resistance was measured both at room temperature and at 4.2K. For glass, the longitudinal resistance R_{xx} was about 1.15kΩ and 1.39kΩ, at 4.2K. As for SiO_2/Si, we obtained about 950Ω at ambient temperature and 1kΩ at liquid helium temperature. Thus, the obtained values were in the range of the values previously reported on CVD-grown graphene[62, 73].

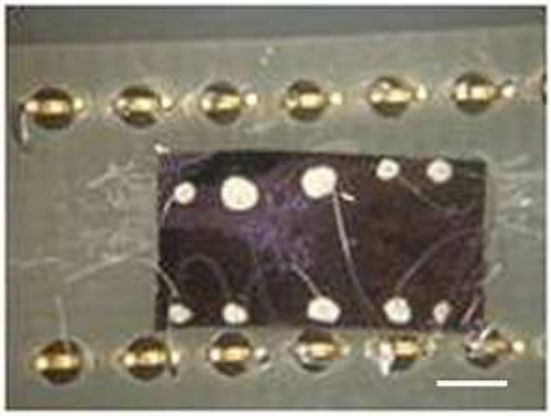

Figure 4.15: Picture of a wired CVD-grown graphene device on chip carrier. (Scale bar: 2.5 mm)

5

Conclusion

This thesis provides a reference for the characterization of the quality of graphene film and a good starting point in the preparation of graphene samples to achieve high-quality electronic devices. We have showed that Raman spectroscopy serves as a powerful tool to distinguish the number of layers of graphene as well as to confirm the presence of strain and disorder in the graphene sheet.

The performance of graphene-based devices is highly sensitive to the substrate used and disorder deteriorates the intrinsic properties of graphene. Highly ordered substrates provide the best solution to optimize its performance but device preparation is difficult due to the difficulty in identifying graphene sheets down to single layer. We have demonstrated that the contrast of graphene monolayers on low-contrast substrate such as GaAs and high-contrast substrate such as SiO_2 is enhanced by simply tilting the sample and light source. We also calculated the contrast using the transfer matrix method and the results agree well with the experimental data.

Our recent work on CVD-grown graphene has provided some insights on the influence of different growth parameters. We presented some of our preliminary results in order to optimize the synthesis of graphene on Cu. First, an increase in temperature results in a large density and size of growth domains. In our Raman analysis, shifts of the 2D peak were observed which we attributed to isotropic compressive strain induced by the Cu during cooling. Double-resonance theory is employed to explain this phenomena as well as a possible explanation of the presence of ripples. Secondly, under prevailing conditions, we observed that graphene has reached full coverage after 15 minutes. For longer growth times, we have not observed the formation of large bilayer

graphene flakes demonstrating that graphene growth on Cu is indeed a self-limited process, as opposed to precipitation-based growth. Finally, we showed that a lack of hydrogen flow in the CVD system leads to defects in the graphene film. Recently, we have succesfully transferred CVD-grown graphene onto non-metallic substrates using PMMA and thermal release tape as a supporting layer. Although a few problems arise from both of these transfer methods, these can be resolved in the future.

A

Calibration of the EBL system

Employing the EBL system is not an easy task. Since the SEM and EBL are not both automatically correlated, a few calibrations must be performed by the user before any lithographic processings. The success of a lithographic process depends on two key components: beam deflection accuracy and stage positioning. Details on the mechanisms of these components are explained in the following sections.

A.1 Beam Deflection Calibration

A calibration of the deflection is necessary to deviate the beam precisely with respect to the position of the features on the substrate. This is realized by tuning the variable potential that is applied on the deflection coils. Fig. A.1 shows the calibrated deflection angle as a function of the z position and the dashed lines represent the size of the sample. For different position z of the sample, the deflection angle θ for fixed sample size changes. Since the applied voltage is related to the deflection angle, the NPGS software computes the conversion factor which is the *Magnification Scale*.

The magnification and the *Working Distance* are parameters that are involved in the calibration step. The magnification sets the *Working Field*, the area in which the electrons irradiate. As the magnification increases, the *Working Field* is limited to a smaller area. In contrast, the *Working Distance* represents the focused point of the sample, this distance can be modified by adjusting the height of the sample holder. For both parameters, if the z position is modified, the *Magnification Scale* needs to be recalculated manually.

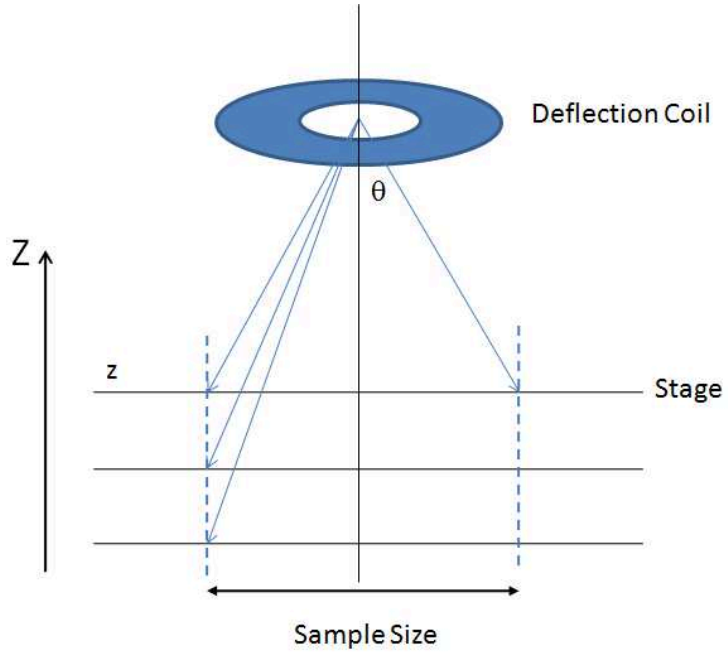

Figure A.1: Diagram of the calibration of the deflection angle as a function of z position.

A.2 Stage Positioning and Sample Alignment

Other mandatory calibrations are the stage positioning and the alignment with predefined structures on the substrate. The user is required to calibrate these parameters for accurate stage movement and lithography. This calibration process is well understood with the concept of reference frames. Two correlations are considered:

1. Correlation between designs and sample.

2. Correlation between sample holder and substrate coordinate systems.

Samples are mounted on a sample holder and then transferred onto the moving stage in the SEM chamber. The SEM hardware controls the stage movement in (x,y) and beam orientation ϕ. However, the height z cannot be regulated; the height of the sample holder can be adjusted manually. The sample of interest is located at some point (x,y) and orientation ϕ. The origin is the central point of the sample holder as sketched in Fig. A.2.

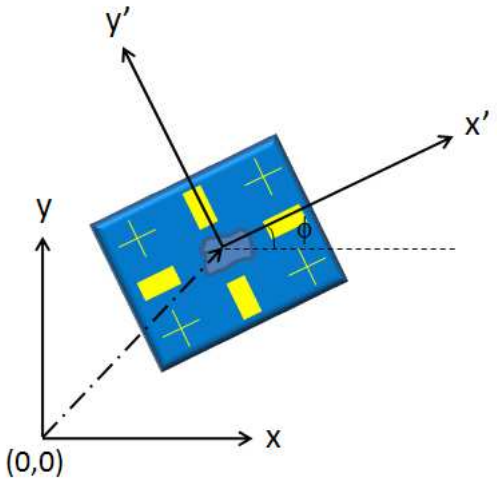

Figure A.2: Reference frames of the sample holder centered at (0,0) and sample of interest at some point (x',y') and orientation ϕ.

The first step is to match the orientation and coordinate system of the substrate with the ones in the designs established by the user. In other words, the (x,y)-axis must align with the (x',y')-axis. This is realized with the aid of alignments marks on the substrate due to the fact that the position, orientation and dimensions of the marks are well-defined. As a consequence, the sample has its own coordinate system (x',y') and the orientation is then corrected by features such as a cross or edge of a bond pad.

The next step is to correlate the stage movement according to the coordinate system of the substrate. In order to avoid any unnecessary exposure of the sample due to SEM imaging, it is desired to start lithography at a spot far away from the sample of interest and NPGS controls the stage movement onto the sample while the beam is off. The automated stage mouvement is calibrated by the user with the use of the *Rotation Matrix* in the NPGS software. This is accomplished by selecting three points of known coordinates on the substrate's coordinate system. The *Direct Stage Control* moves the stage according to the parameters set by the *Rotation Matrix* and the accuracy of the translational movement can then be verified before exposure.

A.3 Working Area

The *Working Area* represents the regions which will be exposed on the PMMA according to the designs. If the dimensions of the pattern fits within the SEM's *Working Field*, no motorized positioning occurs. For large designs, the pattern is divided into smaller pieces that have the dimensions of the *Working Field* shown in Fig. A.3(a). As a consequence, each part of the pattern is exposed individually by automated stage mouvement and a good calibration on the *Rotation Matrix* is necessary for seamless matching of the pattern within the different *Working Fields*. Without proper stage calibration and scaling, the pattern pieces (or the *Working Fields*) overlap or won't stitch with other pieces as seen in Fig. A.3(b).

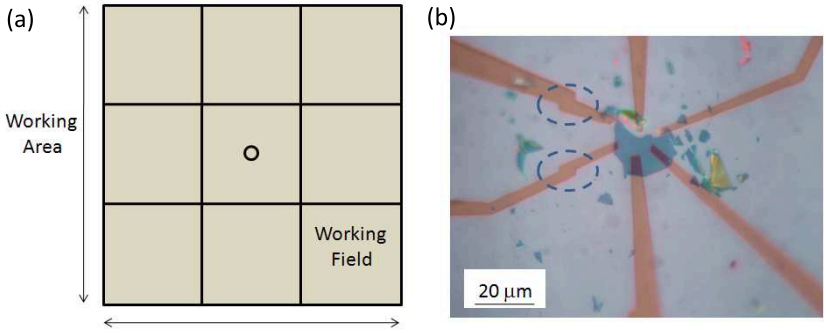

Figure A.3: (a) Relationship between the *Working Area* and the *Working Field*. (b) The pattern is slightly offset from the sample's actual position and the dashed circles show the regions where the pattern overlaps due to lack of proper calibration and scaling.

B

Contacting Sub-nanometers Features: An Alternative Approach

Content

This section presents an alternative method to the Fracture command. The Fracture is purposely used for patterning at large scales. However, it usually lacks precision and the major factor originates from the height of the chuck. According on its height, the magnification scale has to be accurately calculated in order to perform precise lithography. This means previous users should not change the height of the chuck or else the expected results will not be obtained.

In the presented method, one is guaranteed to obtain precise lithography within 1 μm error if the calibration is performed correctly. However, this procedure takes more time than the Fracture command as this method works only for *local* lithography, meaning that the stage will not be moving while patterning. This method is best done if alignments marks are present on the substrate or any features of known dimensions.

Before Electron Beam Lithography

1. Take an image of your sample and scale the image with DesignCad found in the NPGS program. Go to Dimension $\rightarrow$ Dimension to measure horizontally and vertically the length of your alignment marks, then use 's' to scale your image.

2. In the figure below, each gold mark is separated by 100 μm with dimensions of 10 μm x 10 μm. Choose 3 marks which are within a 190 μm x 190 μm window and also furthest from your sample of interest. For each mark, create a layer and assign each layer with a color (ex. Green, Orange, Fushia).

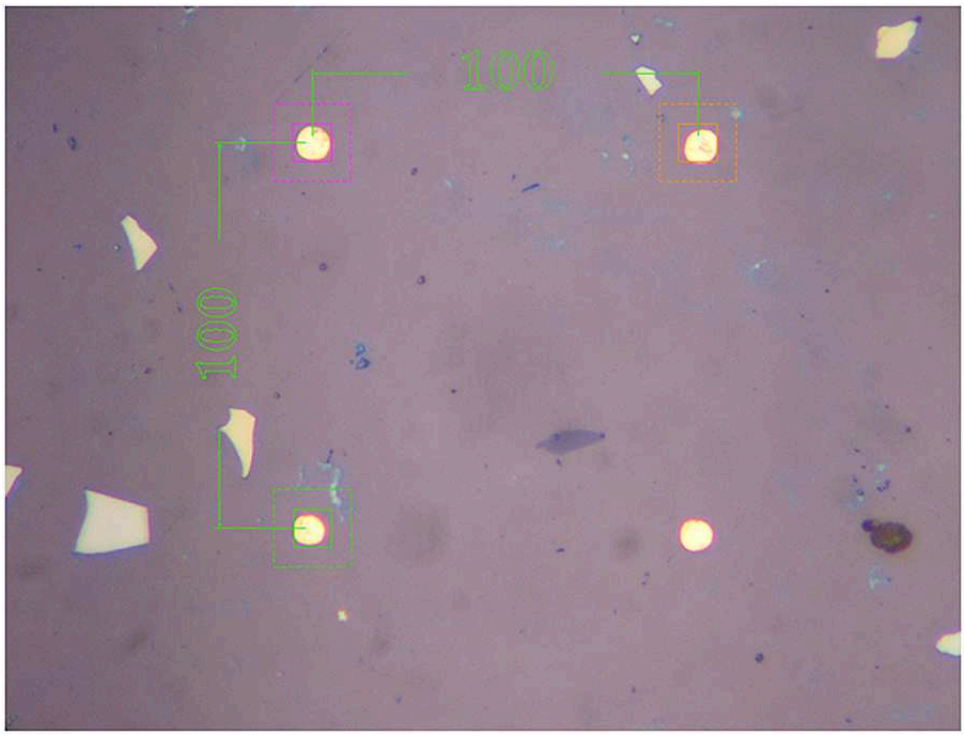

3. Draw a lined-box around each gold mark (ie. 10 μm x 10 μm). Make sure that each mark refers to a layer. Using the PolyFill (PF) command, draw a larger box around each lined-box (ex. 20 μm x 20 μm). This is used to locally scan the area of your substrate in order to align your lined-box with the gold marks in the EBL.

4. Remove image. Use the MaxMag (MM) command then use 'o' to center your origin in between the marks.

5. Save this file. This will be the alignment file.

6. Rename this file which will be the pattern file.

7. 'Ctrl-z' to bring back image. Delete all the dashed-boxes.

8. Draw a 190 μm x 190 μm lined-box centered at (0,0); the EBL can only pattern within this range.

9. Use the PolyFill command to draw the electrodes. EBL can pattern features less than 500nm. Save this file as the pattern file.

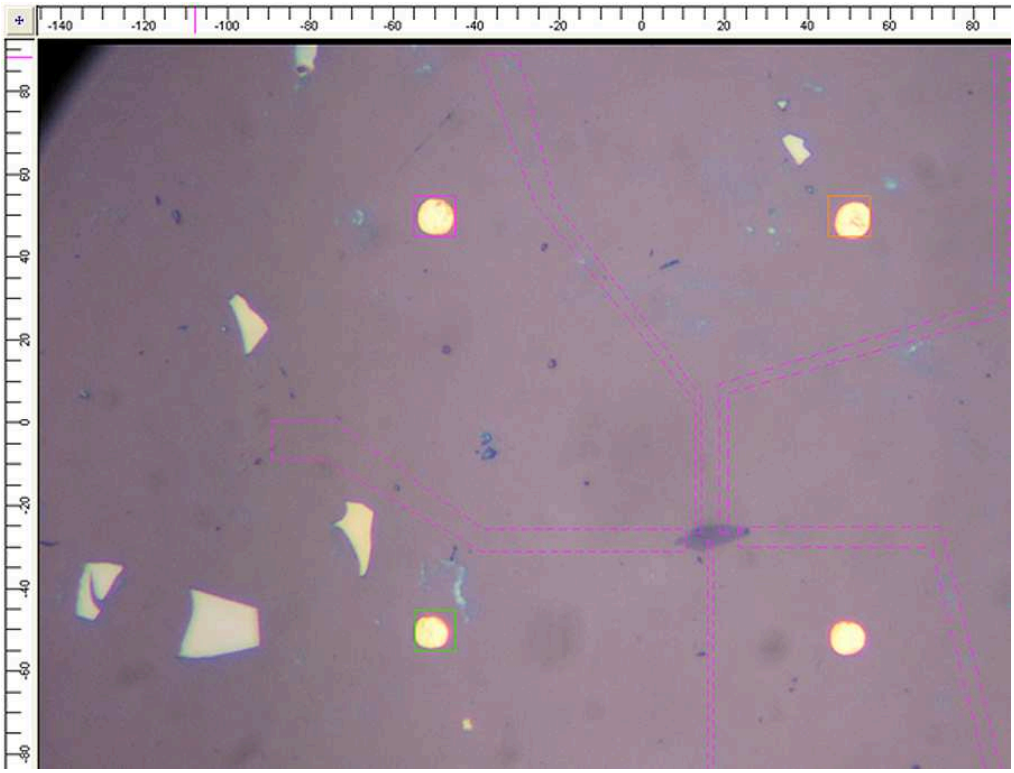

10. The extension of the pads is done using *Fracture* pattern. This part is less critical since no specific features are involved.

11. Take a 10x picture of your sample. Scale your image using 's' and center your (0,0) the same origin as your alignment/pattern file.

12. Draw your pads with the PolyFill command as shown in the figure below. Save this file as your fracture file.

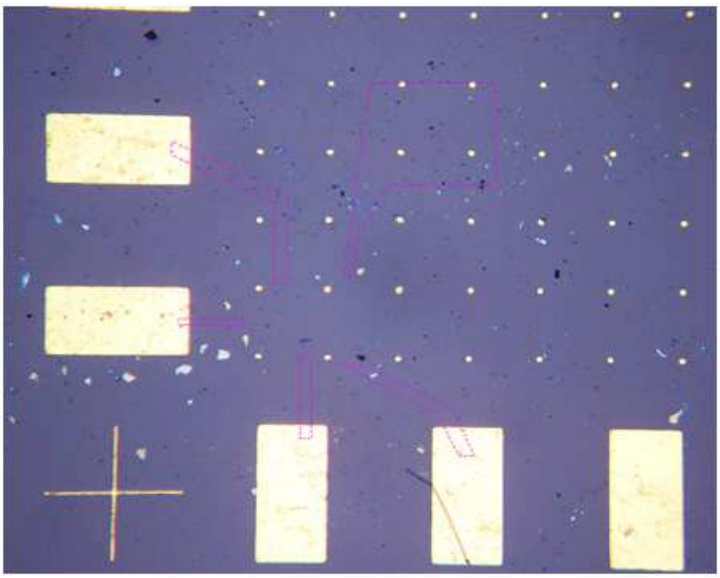

During Electron Beam Lithography - Calibration

1. After ramping the voltage to 30kV and blanking the beam, use the appropriate Condenser Lens in which the probe current is less than 80pA, so electrons won't affect the PMMA much.

2. Go to your alignment marks, far away from your sample and rotate the substrate to align the marks with the crosshairs of the EBL.

3. Perform Rotation Matrix as mentioned in the SYSTEM CALIBRATION.pdf. Make sure that there is not much offset when performing the stage movement. Recalibrate if required.

4. Transfer all your DesignCad Files in your project folder. Open DesignCad Express and save all your DesignCad files (NPGS → Save - Saves to Current NPGS Project).

5. On the NPGS program, check your magnification scale (Options → Pg.sys → mag scale). For reasonable fracture results, I use 95240. As mentioned at the beginning, this value is dependent on the height of the chuck.

6. Go to the NPGS Run File Editor by right-clicking in the DesignCad Files menu. The alignment (R4_C1_2x7-a) and pattern (R4_C1_2x7-s) files will be used as one single executable file. Fill up the following parameters for both files. The current depends on the Cond. Lens used. In the pattern file, the pattern is only written in a fushia layer with an Area Dose of 300.00 C/cm^2.

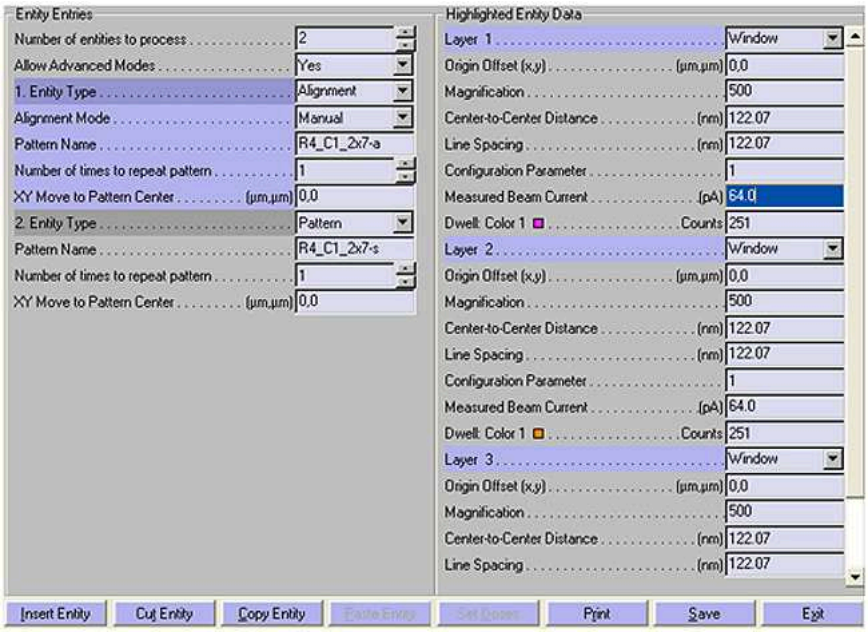

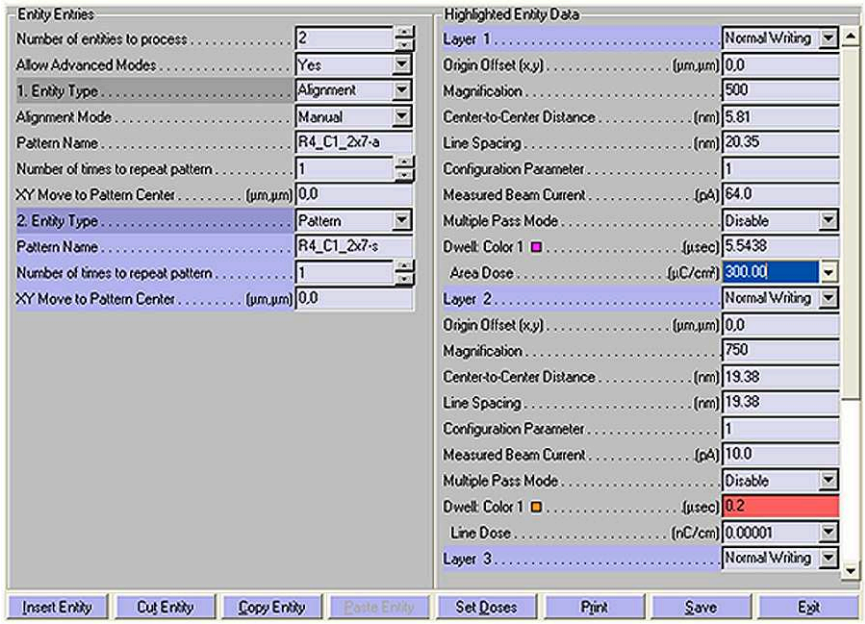

7. Save Run Editor File.

8. Blank the beam (NPGS mode + Beam Off). SEM Magnification : 500x.

9. Using the NPGS program (Commands → Direct Stage Controller) or the stage controller, move to your sample of interest and position the origin (0,0) according to your alignment file.

10. In the Run Files menu, Process Run File. The picture below shows exactly the alignment process in the EBL. NPGS scans the 3 regions and 3 lined-boxes appear. Position each lined-box with the scanned alignment marks. Individual positioning is done by selecting the layer with the 'insert' key.

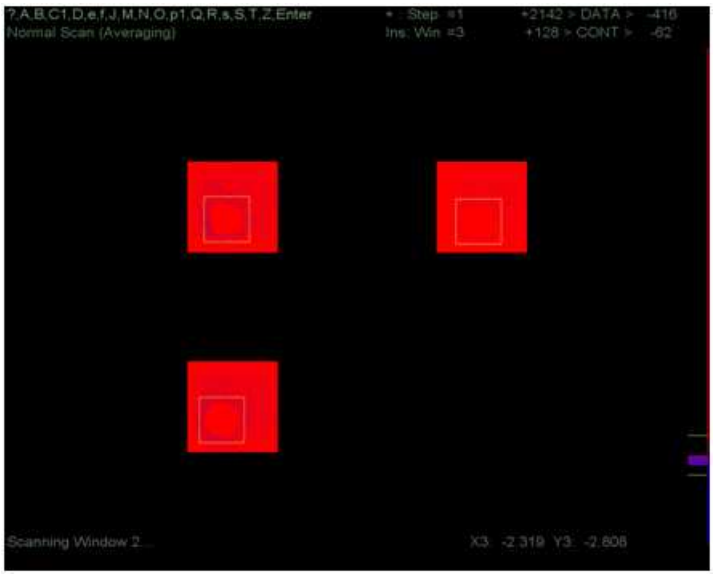

11. Enter and on the top left, it will ask if you want to recalculate matrix before saving. Click Enter or 'y' to reposition, realign to verify if the stage movement is done correctly.

12. Proceed to the pattern file.

13. By now, the pattern near your sample is done. All you need is to extend the pads.

14. Change the following parameters for the fracture file (R4_C1_2x7-fr) in Entity Entries :

    Non-Stop Writing : Yes

    Disable Automated Stage Control : No

    Enable Global Rotation Control : Yes

15. Fill up the following parameters :

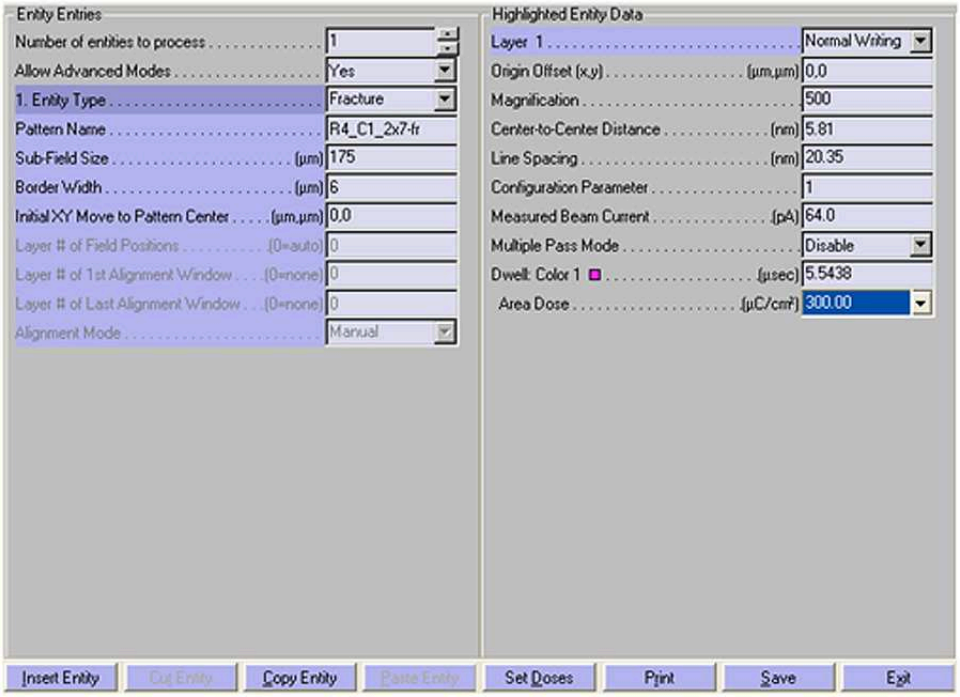

16. Save Run Editor File.

17. If necessary, on the NPGS program, click on Estimate Total Time or Simulate Writing to check if everything is okay before running.

18. Process Run File.

PMMA Development

To develop PMMA, use 1:3 MIBK:IPA and develop for 30 seconds. If underdevelop, develop for 15 additional seconds. A full development is shown in the figure below.

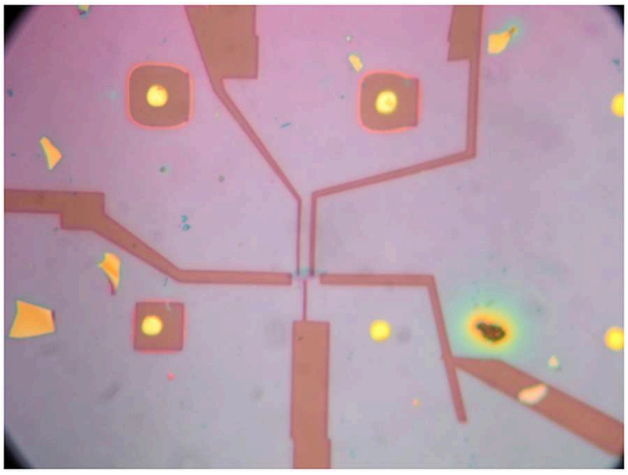

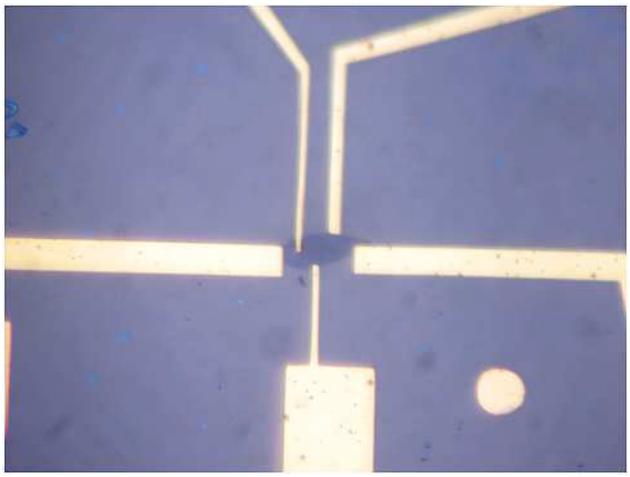

Bibliography

[1] H. W. Kroto, J. R. Heath, S. C. O'Brien, R. F. Curl and R. E. Smalley, Nature **318**, 162 (1985).

[2] S. Iijima, Nature **354**, 56 (1991).

[3] P. R. Wallace, Physical Review **71**, 622 (1947).

[4] N. D. Mermin, Physical Review **176**, 250 (1968).

[5] K. S. Novoselov, D. Jiang, F. Schedin, T. J. Booth, V. V. Khotkevich, S. V. Morozov and A. K. Geim, PNAS **102**, 10451 (2005).

[6] K. S. Novoselov, A. K. Geim, S. V. Morozov, D. Jiang, Y. Zhang, S. V. Dubonos, I. V. Grigorieva and A. A. Firsov, Science **306**, 666 (2004).

[7] K. I. Bolotin, K. J. Sikes, Z. Jiang, M. Klima, G. Fudenberg, J. Hone, P. Kim and H. L. Stormer, Solid State Communications **146**, 351 (2008).

[8] C. Lee, X. Wei, J. W. Kysar and J. Hone, Science **321**, 385 (2008).

[9] K. S. Novoselov, A. K. Geim, S. V. Morozov, D. Jiang, M. I. Katsnelson, I. V. Grigorieva, S. V. Dubonos and A. A. Firsov, Nature **438**, 197 (2005).

[10] Y. Zhang, Y.-W. Tan, H. L. Stormer and P. Kim, Nature **438**, 201-204 (2005).

[11] A. H. Castro Neto, F. Guinea, N. M. R. Peres, K. S. Novoselov and A. K. Geim, Reviews of Modern Physics **81**, 109 (2009).

[12] K. F. Mak, J. Shan, and T. F. Heinz, Phys. Rev. Lett. **104**, 176404 (2010).

[13] R. Saito and M. Dresselhaus, *Physical properties of carbon nanotubes*, Imperial College Press, 1998.

[14] S. V. Morozov, K. S. Novoselov, M. I. Katsnelson, F. Schedin, D. C. Elias, J. A. Jaszczak and A. K. Geim, Physical Review Letters 100, 016602 (2008).

[15] B. Lang, Surface Science **53**, 317 (1975).

[16] D. Chen, L. Tang and J. Li, Chemical Society Reviews **39**, 3157 (2010).

[17] J. Hass, W. A. de Heer, and E. H. Conrad, J. Phys. Cond. Matter **20**, 323202 (2008).

[18] J. Hass, R. Feng, T. Li, X. Li, Z. Zong, W. A. de Heer, P. N. First, E. H. Conrad, C. A. Jeffrey and C. Berger, Applied Physics Letters **89**, 143106 (2006).

[19] K. V. Emtsev, A. Bostwick, K. Horn, J. Jobst, G. L. Kellogg, L. Ley, J. L. McChesney, T. Ohta, S. A. Reshanov, J. Rohrl, E. Rotenberg, A. K. Schmid, D. Waldmann, H. B. Weber and T. Seyller, Nat Mater **8**, 203 (2009).

[20] P. Darancet, N. Wipf, C. Berger, W. A. de Heer and D. Mayou, Physical Review Letters **101**, 116806 (2008).

[21] X. Li, W. Cai, J. An, S. Kim, J. Nah, D. Yang, R. Piner, A. Velamakanni, I. Jung, E. Tutuc, S. K. Banerjee, L. Colombo and R. S. Ruoff, Science **324**, 1312 (2009).

[22] A. Reina, X. Jia, J. Ho, D. Nezich, H. Son, V. Bulovic, M. S. Dresselhaus and J. Kong, Nano Letters **9**, 30 (2008).

[23] A. G. Cano-Marquez, F. J. Rodrguez-Macias, J. Campos-Delgado, C. G. Espinosa-Gonzalez, F. Tristan-Lopez, D. Ramrez-Gonzalez, D. A. Cullen, D. J. Smith, M. Terrones and Y. I. Vega-Cantu, Nano Letters **9**, 1527 (2009).

[24] D. V. Kosynkin, A. L. Higginbotham, A. Sinitskii, J. R. Lomeda, A. Dimiev, B. K. Price and J. M. Tour, Nature **458**, 872 (2009).

[25] L. Jiao, L. Zhang, X. Wang, G. Diankov and H. Dai, Nature **458**, 877 (2009).

[26] Y. W. Tan, Y. Zhang, K. Bolotin, Y. Zhao, S. Adam, E. H. Hwang, S. Das Sarma, H. L. Stormer and P. Kim, Physical Review Letters **99**, 246803 (2007).

[27] C. R. Dean, A. F. Young, I. Meric, C. Lee, L. Wang, S. Sorgenfrei, K. Watanabe, T. Taniguchi, P. Kim, K. L. Shepard, J. Hone, arXiv:1005.4917.

[28] P. Blake, E. W. Hill, A. H. C. Neto, K. S. Novoselov, D. Jiang, R. Yang, T. J. Booth and A. K. Geim, Applied Physics Letters **91**, 063124 (2007).

[29] L. Lei, J. Bai, Y. Qu, Y. Huang and X. Duan, Nanotechnology **21**, 015705 (2010).

[30] I. Jung, M. Pelton, R. Piner, D. A. Dikin, S. Stankovich, S. Watcharotone, M. Hausner and R. S. Ruoff, Nano Letters **7**, 3569 (2007).

[31] G. Teo, H. Wang, Y. Wu, Z. Guo, J. Zhang, Z. Ni and Z. Shen, Journal of Applied Physics **103**, 124302 (2008).

[32] A. Gupta, G. Chen, P. Joshi, S. Tadigadapa and Eklund, Nano Letters **6**, 2667 (2006).

[33] A. C. Ferrari, J. C. Meyer, V. Scardaci, C. Casiraghi, M. Lazzeri, F. Mauri, S. Piscanec, D. Jiang, K. S. Novoselov, S. Roth and A. K. Geim, Physical Review Letters **97**, 187401 (2006).

[34] J. R. Ferraro, K. Nakamoto and C. W. Brown, *Introductory Raman Spectroscopy*, Academic Press ed. (2003).

[35] D. A. Long, *The Raman Effect: A Unified Treatment of the Theory of Raman Scattering by Molecules*, John Wiley & Sons (2001).

[36] http://www.ws.chemie.tu-muenchen.de/groups/haisch/techniques0/raman-microscopy, Retrieved May 21, 2010.

[37] A. C. Ferrari and J. Robertson, Physical Review B **61**, 14095 (2000).

[38] A. C. Ferrari and J. Robertson, Physical Review B **64**, 075414 (2001).

[39] T. Shimada, T. Sugai, C. Fantini, M. Souza, L. G. Canado, A. Jorio, M. A. Pimenta, R. Saito, A. Grneis, G. Dresselhaus, M. S. Dresselhaus, Y. Ohno, T. Mizutani and H. Shinohara, Carbon **43**, 1049 (2005).

[40] L. M. Malard, M. A. Pimenta, G. Dresselhaus and M. S. Dresselhaus, Physics Reports **473**, 51 (2009).

[41] F. Tuinstra and J. L. Koenig, The Journal of Chemical Physics **53**, 1126 (1970).

[42] D. M. Basko, S. Piscanec and A. C. Ferrari, Physical Review B **80**, 165413 (2009).

[43] Y. Wang, Z. Ni, T. Yu, Z. X. Shen, H. M. Wang, Y. H. Wu, W. Chen and A. T. Shen Wee, The Journal of Physical Chemistry C **112**, 10637 (2008).

[44] C. Thomsen and S. Reich, Physical Review Letters **85**, 5214 (2000).

[45] D. Graf, F. Molitor, K. Ensslin, C. Stampfer, A. Jungen, C. Hierold and L. Wirtz, Nano Letters **7**, 238 (2007).

[46] L. G. Canado, A. Reina, J. Kong and M. S. Dresselhaus, Physical Review B **77**, 245408 (2008).

[47] Z. Ni, Y. Wang, T. Yu and Z. Shen, Nano Research **1**, 273 (2008).

[48] J. C. Charlier, X. Gonze and J. P. Michenaud, Physical Review B **43**, 4579 (1991).

[49] D. S. L. Abergel, A. Russell and V. I. Fal'ko, Applied Physics Letters **91**, 063125 (2007).

[50] K. Chang, J. T. Liu, J. B. Xia and N. Dai, Applied Physics Letters **91**, 181906 (2007).

[51] S. Roddaro, P. Pingue, V. Piazza, V. Pellegrini and F. Beltram, Nano Letters **7**, 2707 (2007).

[52] V. Yu and M. Hilke, Applied Physics Letters **95**, 151904 (2009).

[53] M. Born and E. Wolf, *Principles of Optics*, Cambridge University Press (1999).

[54] *Handbook of Optical Constants of Solids*, edited by E. D. Palik (Academic, New York, 1991), Vol. 2.

[55] J. Henrie, S. Kellis, S. Schultz and A. Hawkins, Opt. Express **12**, 1464 (2004).

[56] J. Chilwell and I. Hodgkinson, J. Opt. Soc. Am. A **1**, 742 (1984).

[57] C. Casiraghi, A. Hartschuh, E. Lidorikis, H. Qian, H. Harutyunyan, T. Gokus, K. S. Novoselov and A. C. Ferrari, Nano Letters **7**, 2711 (2007).

[58] R. R. Nair, P. Blake, A. N. Grigorenko, K. S. Novoselov, T. J. Booth, T. Stauber, N. M. R. Peres and A. K. Geim, Science **320**, 1308 (2008).

[59] A. Starodubov, M. Medvetskii, A. Shikin and V. Adamchuk, Physics of the Solid State **46**, 1340 (2004).

[60] J. Coraux, A. T. NDiaye, M. Engler, C. Busse, D. Wall, N. Buckanie, F. Heringdorf, R. van Gastei, B. Poelsema, T. Michely, New J. Phys. **11**, 023006 (2009).

[61] K. S. Kim, Y. Zhao, H. Jang, S. Y. Lee, J. M. Kim, K. S. Kim, J.-H. Ahn, P. Kim, J.-Y. Choi and B. H. Hong, Nature **457**, 706 (2009).

[62] S. Bae, H. Kim, Y. Lee, X. Xu, J.-S. Park, Y. Zheng, J. Balakrishnan, T. Lei, H. Ri Kim, Y. I. Song, Y.-J. Kim, K. S. Kim, B. Ozyilmaz, J.-H. Ahn, B. H. Hong and S. Iijima, Nat. Nanotechnol. **5**, 574 (2010).

[63] Q. Yu, J. Lian, S. Siriponglert, H. Li, Y. P. Chen and S.-S. Pei, Applied Physics Letters **93**, 113103 (2008).

[64] X. Li, W. Cai, L. Colombo and R. S. Ruoff, Nano Letters **9**, 4268 (2009).

[65] T. M. G. Mohiuddin, A. Lombardo, R. R. Nair, A. Bonetti, G. Savini, R. Jalil, N. Bonini, D. M. Basko, C. Galiotis, N. Marzari, K. S. Novoselov, A. K. Geim and A. C. Ferrari, Physical Review B **79**, 205433 (2009).

[66] G. Tsoukleri, J. Parthenios, K. Papagelis, R. Jalil, A. C. Ferrari, A. K. Geim, K. S. Novoselov and C. Galiotis, Small **5**, 2397-2402 (2009).

[67] P. A. Khomyakov, G. Giovannetti, P. C. Rusu, G. Brocks, J. van den Brink and P. J. Kelly, Physical Review B **79**, 195425 (2009).

[68] V. M. Karpan, P. A. Khomyakov, A. A. Starikov, G. Giovannetti, M. Zwierzycki, M. Talanana, G. Brocks, J. van den Brink and P. J. Kelly, Physical Review B **78**, 195419 (2008).

[69] M. M. Lucchese, F. Stavale, E. H. M. Ferreira, C. Vilani, M. V. O. Moutinho, R. B. Capaz, C. A. Achete and A. Jorio, Carbon **48**, 1592-1597 (2010).

[70] M. Zhu, J. Wang, B. C. Holloway, R. A. Outlaw, X. Zhao, K. Hou, V. Shutthanandan and D. M. Manos, Carbon **45**, 2229 (2007).

[71] S. J. Chae, F. Güneş, K. K. Kim, E. S. Kim, G. H. Han, S. M. Kim, H.-J. Shin, S.-M. Yoon, J.-Y. Choi, M. H. Park, C. W. Yang, D. Pribat and Y. H. Lee, Advanced Materials **21**, 2328 (2009).

[72] X. Li, Y. Zhu, W. Cai, M. Borysiak, B. Han, D. Chen, R. D. Piner, L. Colombo and R. S. Ruoff, Nano Letters **9**, 4359 (2009).

[73] H. Cao, Q. Yu, L. A. Jauregui, J. Tian, W. Wu, Z. Liu, R. Jalilian, D. K. Benjamin, Z. Jiang, J. Bao, S. S. Pei and Y. P. Chen, Applied Physics Letters **96**, 122106 (2010).